

2016

# The Numerical Solution of the Helmholtz Equation for the Bloodcell Shape: Mars Project

Jill Kelly Resh

Roger Williams University, [jresh123@rwu.edu](mailto:jresh123@rwu.edu)

Follow this and additional works at: [http://docs.rwu.edu/math\\_theses](http://docs.rwu.edu/math_theses)



Part of the [Mathematics Commons](#)

---

## Recommended Citation

Resh, Jill Kelly, "The Numerical Solution of the Helmholtz Equation for the Bloodcell Shape: Mars Project" (2016). *Mathematics Theses*. Paper 2.

[http://docs.rwu.edu/math\\_theses/2](http://docs.rwu.edu/math_theses/2)

This Thesis is brought to you for free and open access by the Feinstein College of Arts and Sciences Theses at DOCS@RWU. It has been accepted for inclusion in Mathematics Theses by an authorized administrator of DOCS@RWU. For more information, please contact [mwu@rwu.edu](mailto:mwu@rwu.edu).

**The Numerical Solution of the Helmholtz Equation for  
the Bloodcell Shape: Mars Project**

**Jill Kelly Resh**

Advisor: Dr. Yajni Warnapala

Bachelor of Science

Department of Mathematics

Feinstein College of Arts and Sciences

Roger Williams University

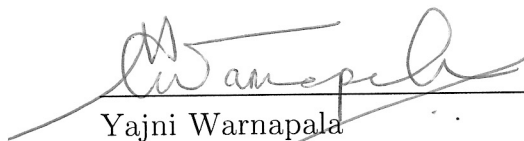
May 2016

The thesis entitled, "The Numerical Solution of the Helmholtz Equation for the Bloodcell Shape: Mars Project," by Jill Resh was reviewed and approved by the following:

  
\_\_\_\_\_  
Jill Resh

Author

Date 4/29/16

  
\_\_\_\_\_  
Yajni Warnapala

Chairperson of the Department of Mathematics  
Thesis advisor

Date 28<sup>th</sup> of April '16

  
\_\_\_\_\_  
Robert Eisinger

Professor and Dean, College of Arts and Sciences

Date 2 MAY 2016

This thesis is dedicated in loving memory of my brother, John B. Resh, who was my motivation  
in the most trying times.

This thesis is also dedicated to my advisor, Dr. Yajni Warnapala, and my parents, Franklin and  
Catharine Resh.

## *Acknowledgements*

I would like to thank Professor Earl Gladue, Dr. Bruce Burdick, and Professor Sharon DeLucca for being part of my thesis committee and helping to make this thesis successful. I would also like to thank Mrs. Patricia Kennedy for her continued help and technical support.

I would like to thank the EPSCoR Grant and Jim Lemire, The Rhode Island NASA Space Grant, the Newport Naval Warfare Center, and the Roger Williams University Department of Mathematics for funding this thesis. I would like to extend my gratitude to the Roger Williams University Provost Fund and the Mathematical Association of America (MAA) travel fund for funding the travel expenses involved in presenting my research.

I would like to thank Dr. Marcie Marston for organizing the Mathematics and Science senior thesis schedule and presentations this year.

I would like to thank my parents and my sister for believing in me and cheering me on, Joseph Martin III for pushing me to do better, and my friends for their emotional support.

Finally, I would like to extend my gratitude to my thesis advisor, mentor, and professor, Dr. Yajni Warnapala for providing me the opportunity to research with her and helping me every step of the way. Without Dr. Warnapala, this thesis would not have been possible.

# Contents

<b>1</b>	<b>Literature Review</b>	<b>1</b>
<b>2</b>	<b>Introduction</b>	<b>4</b>
<b>3</b>	<b>Science of Planet Mars</b>	<b>9</b>
<b>4</b>	<b>Numerical Methods</b>	<b>14</b>
4.1	Modified Galerkin Method . . . . .	15
<b>5</b>	<b>Proof of Green's Theorem</b>	<b>19</b>
<b>6</b>	<b>Proof of Laplace's Equation Solution</b>	<b>21</b>
<b>7</b>	<b>Numerical Results</b>	<b>24</b>
7.1	Convergence Results: Boundary Function One . . . . .	27
7.2	Convergence Results: Boundary Function Two . . . . .	31
<b>8</b>	<b>Conclusion</b>	<b>38</b>
<b>9</b>	<b>Possible Future Directions for this Work</b>	<b>41</b>
<b>10</b>	<b>Appendix A</b>	
	<b>Definitions</b>	<b>42</b>
10.1	Basis . . . . .	42
10.2	Bessel Functions . . . . .	42
10.3	$C^{l,\lambda}$ space . . . . .	43

10.4	Hankel Functions . . . . .	43
10.5	Infinite Space . . . . .	43
10.6	Jacobian . . . . .	44
10.7	Legendre Functions . . . . .	44
10.8	Norm . . . . .	45
10.9	Smoothness . . . . .	45
10.10	Uniform Continuity . . . . .	45
10.11	Uniform Convergence . . . . .	45
<b>11</b>	<b>Appendix B</b>	
	<b>Proofs and Examples</b>	<b>46</b>
11.1	Proof of Spherical Harmonic Basis . . . . .	46
11.2	Proof of Galerkin's Weighted Residual Method . . . . .	46
11.3	Example: Adomian Decomposition Method . . . . .	49
11.4	Example of the Modified Decomposition method . . . . .	50
<b>12</b>	<b>Appendix C</b>	
	<b>Figures</b>	<b>52</b>
<b>13</b>	<b>References</b>	<b>56</b>

# List of Figures

2.1	Illustration of the Biconcave Disk with its cross section displayed. . . . .	6
2.2	The Biconcave Disk with the ellipsoid inscribed inside. . . . .	7
3.1	Stratification of the planet Mars atmosphere. . . . .	9
3.2	Photograph of the 3-D model of the Bloodcell. . . . .	12
7.1	Change in shape as $C$ decreases. . . . .	25
12.1	The Biconcave Disk programmed into the Neumann boundary condition program. . .	54
12.2	Some of the Gaussian Quadrature weights and nodes in the Neumann boundary condition program. . . . .	55

# List of Tables

2.1	Convergence results for tested equations of the $z$ -coordinate. . . . .	8
3.1	Table of wavenumber calculations. . . . .	11
7.1	Convergence results for tested values for $C$ . . . . .	25
7.2	Convergence results for very low wavenumbers. . . . .	26
7.3	Convergence results for degree of boundary function 1. . . . .	27
7.4	Convergence results for number of nodes of boundary function 1. . . . .	29
7.5	Convergence results for degree of boundary function 2. . . . .	31
7.6	Convergence results for number of nodes of boundary function 2. . . . .	33



7.7	Convergence results of calculated wavenumbers for boundary function 2. . . . .	35
7.8	Convergence results for the Dirichlet eigenvalue: boundary function1 and boundary function 2. . . . .	37
8.1	Study of the effects of drag coefficient on the Biconcave Disk. . . . .	39
12.1	Data table of atmospheric conditions on planet Mars from a report on the MOLA mission. . . . .	53

## List of Graphs

7.1	Convergence results for degree of boundary function 1. . . . .	28
7.2	Convergence results for degree of boundary function 1. . . . .	30
7.3	Convergence results for degree of boundary function 2. . . . .	32
7.4	Convergence results for number of nodes of boundary function 2. . . . .	34
7.5	Convergence results of calculated wavenumbers for boundary function 2. . . . .	36

## **Abstract**

The objective of this research is to investigate numerical solutions of several boundary value problems for the Helmholtz equation for the shape of a Biconcave Disk. The boundary value problems this research mainly focuses on are the Neumann and Robin boundary problems. The Biconcave Disk is a closed, simply connected, bounded shape modified from a sphere where the two sides concave toward the center, mapped by a sine curve. There are some numerical issues in this type of analysis; any integration is affected by the wave number  $k$ , because of the oscillatory behavior of the fundamental solution of the Helmholtz equation. This project was funded by NASA RI Space Grant and the NASA EPSCoR Grant for testing of boundary conditions for the Biconcave Disk. This method has already been investigated for the sphere, ellipsoid, superellipsoid, and the oval of cassini. The primary purpose of this research is to extend those known results to the Biconcave Disk with calculating the possibility of this shape acquiring sufficient conditions to be part of a spacecraft that might one day land on planet Mars.

# 1. *Literature Review*

Laplace's equation is an elliptic partial differential equation first studied by Pierre-Simon Laplace (Weisstein, n.d.). It is given by  $\Delta u = 0$ , where  $\Delta$  is the Laplacian operator and  $u$  is a scalar function. Laplace's equation is a particular case of the Helmholtz Equation,  $\Delta u + k^2 u = 0$ , with  $\text{Im } k = 0$ . Laplace's equation can be solved by separation of variables (proof in Section 6). Harmonic functions are solutions to Laplace's equation. These functions also have the property that the average value over the surface is the same as the value at the center of the shape. Dirichlet and Neumann boundary conditions can be used to solve Laplace's equation (Weisstein, n.d.).

Integrals that arise from the separation of variables method for partial differential equations may not always be solvable (Kropinski and Quaife, 2010). When this happens, the collocation method is used to approximate a solution. The collocation method uses a finite sum to approximate a definite integral (Frank, n.d.). This creates a quadrature rule formed of weighted quadrature nodes for the given function. Adding more nodes to the quadrature allows for more precision, thus a better approximation of the true solution. Furthermore, different collocation methods have different limitations that may lead to a better or worse approximation (Frank, n.d.).

The finite element method is frequently used to solve partial differential equations. This method approximates unknown variables to transform a partial differential equation into a system of algebraic equations, and it can be extended to the study of a heterogeneous environment. Richard Courant proposed the idea of the finite element method in 1943 (Süli, 2012). His work was later discovered by engineers, who recognized the importance of such approximations to their work.

To use the finite element method to approximate Laplace's equation, first let  $\Delta = \sum_{i=1}^n \frac{\partial^2}{\partial x_i^2}$ , and then a finite element approximation can be obtained for Laplace's equation. As explained previously, a boundary condition is typically used in conjunction with Laplace's equation. Each boundary condition slightly changes the finite element approximation.

The Galerkin method is a way to determine the coefficients of the power series for the finite element method. The coefficients arise from the trial solution and the basis chosen for the given problem. The Galerkin method is the foundation for the finite element method (Süli, 2012).

We use the Galerkin method for our problem because it allows for nodes of varying distance, which is necessary to evaluate over the surfaces of the spherical shapes studied (Kropinski and Quaife, 2010). The Modified Galerkin method adds an infinite series to the fundamental solution of the Helmholtz equation. The infinite series removes the discontinuity that occurs as the distance from the surface,  $r$ , gets very small. The fundamental solution of the Helmholtz equation is  $u = \frac{e^{ikr}}{r}$ , thus if the point is very close to the surface of the shape then  $r$  is very small. If  $r$  gets too small, the fundamental solution approaches infinity, creating a weak singularity. The Modified Galerkin method removes this weak singularity.

In 1982, Kleinman and Roach (1982) proposed choices of coefficients  $a_{nm}$  for the exterior problems for the Helmholtz equation. The basis used to find these coefficients is the spherical harmonics.

In 2002, Lin and Warnapala-Yehiya found numerical solutions for the exterior Dirichlet problem, which is  $u(p) = f(p)$ , for  $p \in S$  such that  $S$  is a closed, bounded surface in  $\mathbb{R}^3$ . The shapes evaluated in this research were the sphere, perturbations of the sphere, and the ellipsoid. In each case, the absolute error converged quickly. They also found that with more terms added to the infinite series, the absolute error becomes smaller (Lin and Warnapala-Yehiya, 2002). Then in 2004, Lin and Warnapala-Yehiya found numerical solutions for the exterior Neumann problem for these same shapes. Again, the absolute error on the boundary of these shapes converged quickly, even for points that were close to the surface (Lin and Warnapala-Yehiya, 2004). For the Neumann problem, they

used coefficients of  $a_{nm} = -\frac{1}{2} \left( \frac{j_n(kR)}{h_n^{(1)}(kR)} + \frac{j_n'(kR)}{h_n^{(1)'}(kR)} \right)$ , and

$a_{nm} = -\frac{1}{2} \left( \frac{j_n(kR)}{h_n^{(1)}(kR)} \right)$ , for  $n = 0, 1, 2, \dots$ , and  $m = -n, \dots, n$ . They had better results with the former (Lin and Warnapala-Yehiya, 2004).

In 2008, Warnapala and Morgan found numerical solutions of the exterior Dirichlet problem for the Helmholtz equation for the Oval of Cassini. The choice of coefficients for this problem was  $a_{nm} = -\frac{1}{2} \left( \frac{j_n(kR)}{h_n^{(1)}(kR)} + \frac{j_n'(kR)}{h_n^{(1)'}(kR)} \right)$ , for  $n = 0, 1, 2, \dots$ , and  $m = -n, \dots, n$ . This problem focused on the exterior Dirichlet problem for the Helmholtz equation (Warnapala and Morgan, 2008). The results were very good, with an absolute error of  $4.298 \times 10^{-4}$  for points as close to the boundary

of the surface as (2, 3, 4). After finding these results, Warnapala and Morgan (2008) accounted for eccentricity of the Oval of Cassini in the coefficient  $a_{nm}$ , and the results were similarly good.

In 2013, Warnapala and Dinh found numerical solutions to the Dirichlet problem for the Superellipsoid for monoharmonic waves on planet Mars. The superellipsoid gave good convergence results for small wave numbers, thus it was deduced that this method is a viable method for testing wavenumbers that arise from the atmospheric conditions on planet Mars (Warnapala and Dinh, 2013). Then in 2014, Warnapala and Dinh found numerical solutions to the exterior Impedance problem for the Superellipsoid by using the Robin boundary condition. The Robin condition is a combination of both the Dirichlet and the Neumann boundary conditions, and it is given by  $\lambda u(p) + \frac{\partial u(p)}{\partial v_p} = f(p)$ ,  $p \in S$ . The coefficients of the infinite series were given to be  $a_{nm} = -\frac{1}{2} \left( \frac{j_n(kR)}{h_n^{(1)}(kR)} + \frac{j_n'(kR)}{h_n^{(1)'}(kR)} \right)$ , for  $n = 0, 1, 2, \dots$ , and  $m = -n, \dots, n$ . This research found that points further from the boundary of the Superellipsoid, especially in the  $z$ -direction, led to better convergence results. Furthermore, it was determined that smaller wavenumbers would generally yield better convergence results (Warnapala and Dinh, 2014). The convergence results were good; however, the absolute error was larger compared to the Dirichlet condition for the Superellipsoid.

Preliminary results for the Biconcave Disk were published by Warnapala, Dinh, and Resh in August of 2015.

## 2. *Introduction*

This research involves studying the theories and equations behind the numerical approximation methods in numerical analysis for solving integral equations, specifically Fredholm inetgral equations of the second kind. The methods, including the Modified Galerkin Method, are applied in a program for numerical solutions to the Helmholtz equation, which was written in Fortran 77. Some of the subroutines used in the program were obtained from the Newport Naval Warfare Center. For diagrams, pictures, and graphs, Maple, Scientific Word, SolidWorks, Microsoft Excel, and Adobe Illustrator were used.

The objective of this work is to find the numerical solution of the Neumann boundary conditions for the Helmholtz equation for a smooth Biconcave Disk (bloodcell). The Helmholtz equation is given by

$$\Delta u + k^2 u = 0, \text{Im } k \geq 0 \quad (2.1)$$

where  $k$  is the wavenumber. The Helmholtz equation is a partial differential equation that is a modification of the wave equation for the case when the waves are monoharmonic. This equation is used in many scattering problems. Neumann boundary conditions are partial differential equation boundary conditions which give the normal derivative of a function on the surface. The exterior Neumann problem for the Helmholtz equation is

$$\frac{\partial u(p)}{\partial v_p} = f(p) \quad (2.2)$$

Where  $p \in S$  and  $f(p)$  can be

$$f_1(p) = \frac{e^{ikr}}{r} \quad (2.3)$$

$$f_2(p) = \frac{e^{ikr}}{r^2} \left(1 + \frac{i}{kr}\right) z \quad \text{or} \quad (2.4)$$

$$f_3(p) = \frac{e^{ikr}}{r^3} \left(-1 + \frac{3}{k^2 r^2} - \frac{3i}{kr}\right) 0.5(3z^2 - r^2) \quad (2.5)$$

where  $r = \sqrt{x^2 + y^2 + z^2}$ . We refer to each function  $f_n$  as boundary function  $n$ , later in this paper. By using the Neumann boundary condition, we assumed that all incoming waves were completely reflected.

The Biconcave Disk is closed, simply connected, and bounded. A key feature of this shape is that it is smooth, thus differentiable. As the Modified Galerkin method is based on the Green's theorem, I will only consider the boundary of the Biconcave Disk. The Biconcave Disk shape is modified from a sphere in that two of the sides are concave toward the center. A formula for these shapes is:

$$\begin{aligned} x &= A \sin(\varphi) \cos(\theta) \\ y &= B \sin(\varphi) \sin(\theta) \\ z &= C \left( \left(1 - \frac{\lambda}{2}\right) + \frac{\lambda}{2} \sin(\varphi) \right) \cos(\varphi) \end{aligned} \quad (2.6)$$

where  $0 < \lambda < 2$ , and  $A$ ,  $B$ , and  $C$  are any constant, with  $0 \leq \theta < 2\pi$  and  $0 \leq \varphi < \pi$ .

Depending on the coefficients  $A$  and  $B$ , the symmetry of the shape will vary, which will affect the drag coefficient, which in turn will have an impact on the orientation of the spacecraft while landing and taking off. In the formula  $A$ ,  $B$ ,  $C$ , and  $\lambda$  are changed to find a shape that exhibits the best convergence, which means that the absolute error approaches zero. The shape that has the lowest absolute error exhibits the best convergence to the fundamental solution. Good convergence results imply that the shape is most likely the best for use as part of a spacecraft.



**Figure 2.1.** An illustration of the Biconcave Disk with its cross section displayed. The bloodcell has the constants  $A = 1$ ,  $B = 1$ ,  $C = 0.55$ , and  $\lambda = 1.4$ .

The formula for the Biconcave Disk (Figure 2.1) was obtained by running tests of a few different  $z$ -equations that map the concavity using different sine and cosine curves. The  $z$ -equation that gave one of the best convergences was:

$$z = C \left( \left( 1 - \frac{\lambda}{2} \right) + \sin(\varphi) \right) \cos(\varphi) \quad (2.7)$$

(Table 2.1). However, the shaped formed using this equation was too spherical. Thus, the equation was changed to

$$z = C \left( \left( 1 - \frac{\lambda}{2} \right) + \frac{\lambda}{2} \sin(\varphi) \right) \cos(\varphi) \quad (2.8)$$

This equation exhibited similar convergence results as Equation 2.6 but created a shape that was more Bloodcell-like, with a deeper depression.

The radius used to approximate the solutions to the Helmholtz equation via the Modified Galerkin method was that of the unit sphere,  $R = 1$ , at the beginning of this research. Only at the edges of the  $xy$ -plane is the radius  $R = 1$  a close approximation to the radius of the Biconcave Disk. Thus, this is not a sufficient approximation of the Biconcave Disk's radius. Therefore, the radius was changed to the radius of an ellipsoid that can be inscribe inside of the Biconcave Disk (see Figure 2.2). The ellipsoid proposed is defined by the following equations:

$$x = A \sin(\varphi) \cos(\theta)$$



$$y = B \sin(\varphi) \sin(\theta) \tag{2.9}$$

$$z = 0.165 \cos(\varphi)$$

where  $A$  and  $B$  are any constant, with  $0 \leq \theta < 2\pi$  and  $0 \leq \varphi < \pi$ . The equation of the radius for the above ellipsoid is given by

$$R = \sqrt{(1 - 0.972775 \cos^2(\varphi))} \tag{2.10}$$

This radius, when used in the program, produced the same numerical results as the radius of 1, as discussed further in Section 7.

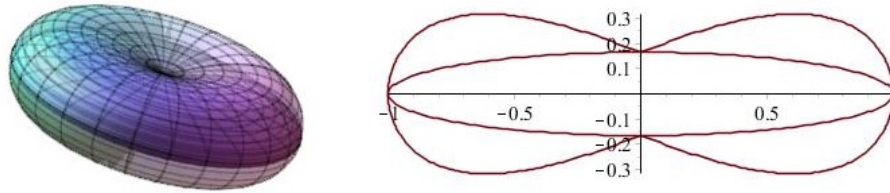


**Figure 2.2.** (left) The Biconcave Disk with  $A = 1$ ,  $B = 1$ ,  $C = 0.55$  and  $\lambda = 1.4$ . The ellipsoid inside the Biconcave Disk is the shape I used to approximate the radius in my calculations by using a its radius (Equations 2.9 and 2.10). (right) A cross-section of the Biconcave Disk with the ellipsoid cross-section inside. From the above figure, we can see that the ellipsoid's radius is a viable approximation to the radius of the Biconcave Disk.

z	Absolute Error
$\left(\left(1 - \frac{\lambda}{2}\right) - \sin(2\varphi)\right) \cos(\varphi)$	3.134D-04
$\left(\left(1 - \frac{\lambda}{2}\right) - \cos(\varphi)\right) \cos(\varphi)$	2.764D-04
$\left(\left(1 - \frac{\lambda}{2}\right) + \sin(2\varphi)\right) \cos(\varphi)$	2.197D-04
$\left(\left(1 - \frac{\lambda}{2}\right) - \sin(\varphi)\right) \cos(\varphi)$	2.049D-04
$\left(\left(1 - \frac{\lambda}{2}\right) + \cos(\varphi)\right) \cos(\varphi)$	2.033D-04
$\left(\left(1 - \frac{\lambda}{2}\right) - \cos(2\varphi)\right) \cos(\varphi)$	8.494D-05
$\left(\left(1 - \frac{\lambda}{2}\right) + \cos(2\varphi)\right) \cos(\varphi)$	4.588D-05
$\left(\left(1 - \frac{\lambda}{2}\right) - \frac{\lambda}{2}\right) \cos(\varphi)$	1.910D-05
$\left(\left(1 - \frac{\lambda}{2}\right) + \frac{\lambda}{2} \sin(\varphi)\right) \cos(\varphi)$	1.808D-06
$\left(\left(1 - \frac{\lambda}{2}\right) + \sin(\varphi)\right) \cos(\varphi)$	9.295D-07

**Table 2.1.**  $N=0,5$ ;  $k=1$ ;  $\lambda=0.4$  were used; number of interior nodes was 16; number of exterior nodes was 8; point (1,2,3000). The boundary function is  $f(p) = e^{ikr}/r$ . Various z-values were tested that mapped the Biconcave Disk, and the one with the best convergence result was chosen to be used for my research.

Because the method is based on Green's Theorem, it is important to note that the surface area and volume of the Biconcave Disk have a closed form for  $A = 1$ ,  $B = 1$ ,  $C = 0.55$ , and  $\lambda = 1.4$ . Given the parameters of the Biconcave Disk (Equation 2.6), the surface area of this Bloodcell is approximately  $8.428369984m^2$  and the volume is approximately  $2.983817832m^3$ . One can find the surface area and volume for any Biconcave Disk shape given its values of  $A$ ,  $B$ ,  $C$ , and  $\lambda$ , thus the Modified Galerkin method is a viable method for evaluation over the surface of the Biconcave Disk.

### 3. *Science of Planet Mars*

The atmosphere on planet Mars is one-hundred times thinner than Earth's atmosphere, and the Martian atmosphere is ninety-five percent carbon dioxide. The atmosphere is thick enough to support weather, wind, and clouds. In fact, the atmosphere on planet Mars is so windy that it creates many dust storms. The average temperature on the surface of Mars is negative eighty degrees Fahrenheit.

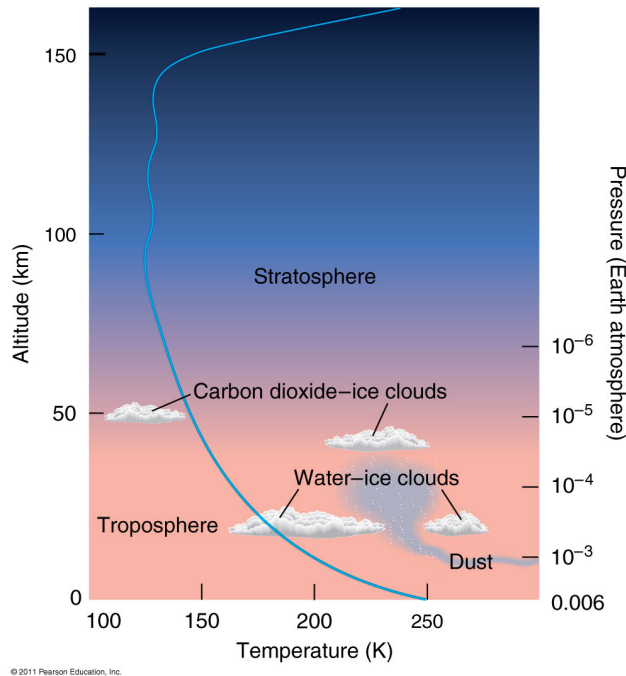


**Figure 3.1.** The temperature and pressure of the Martian atmosphere vary with altitude. <http://pages.uoregon.edu/jimbrou/astr121/Notes/Exam2rev.html>

Mars' atmosphere is mostly carbon dioxide. This is one reason that the atmosphere of Mars is so much different from the atmosphere of Earth, since Earth's atmosphere mostly consists of nitrogen and oxygen. The average air pressure on Earth is 29.92 inches of mercury compared to 0.224 inches of mercury on Mars. Air pressure on Earth varies only slightly compared to air pressure on Mars.

On Earth, there is only about ten percent variation of pressure; whereas on Mars, air pressure varies as much as fifty percent.

The average atmospheric density on Earth is  $1.2256\text{kg}/\text{m}^3$ , which is much higher than Mars at  $0.0155\text{kg}/\text{m}^3$ . Gravity on Earth is over three times the gravity on Mars;  $9.8\text{m}/\text{s}^2$  versus  $3.7\text{m}/\text{s}^2$ , respectively.

Mars has three distinct atmospheric layers: the exosphere, stratosphere, and troposphere. Each layer has its own distinct properties, including density, pressure, and gravity. These properties are important to consider in this research because the wavenumber,  $k$ , is dependent on wavelength by the equation

$$k = \frac{2\pi}{\lambda} \quad (3.1)$$

where  $\lambda$  is the wavelength. The wavenumber is a scalar quantity (radians/meter) that specifies the phase change per meter for a wave. Since wavelength values have not been reported for planet Mars, the wavenumbers were extrapolated from the current atmospheric data reported for planet Mars. The atmospheric data for planet Mars was acquired from a report on the findings of the NASA Viking lander mission. Wavelength in the Mars atmosphere was not reported, so wavenumber was calculated using the formula:

$$k = 2\pi f \sqrt{\frac{\rho}{\gamma P}} \quad (3.2)$$

where  $\rho$  is the atmospheric density,  $P$  is the atmospheric pressure,  $\gamma$  is the adiabatic index, and  $f$  is the frequency, as shown by Dinh (2015). Table 3.1 shows the data used to calculate various wavenumbers on planet Mars via the formula above.

Altitude ( <i>km</i> )	Atmospheric Pressure ( <i>mb</i> )	Atmospheric Density ( <i>kg/m<sup>3</sup></i> )	Frequency ( <i>km/s</i> )	Wavelength ( <i>km</i> )	Wavenumber
131	$1.10E - 07$	$3.53E - 10$	$1.00E + 00$	20	0.31416
108	$4.02E - 06$	$1.66E - 08$	$3.93E - 01$	45	0.13963
80	$2.73E - 04$	$1.47E - 06$	$6.45E - 01$	24	0.26180
62	$5.52E - 03$	$2.47E - 05$	$8.49E - 01$	20	0.31416
42	$7.24E - 02$	$2.28E - 04$	$5.91E - 01$	34	0.18480
23	$6.33E - 01$	$1.79E - 03$	$1.07E + 00$	20	0.31416

**Table 3.1.** This table displays the data used to calculate the wavenumbers that occur in the atmosphere on planet Mars. The atmospheric pressure, density, and wavelength were obtained from the Viking Lander 1 mission. This data was used to calculate the frequencies and subsequently the wavenumbers in the atmosphere. The Adiabatic Index on planet Mars is constant at 1.29. The altitude, which is the distance above the surface of planet Mars, was corrected based on the MOLA findings (Withers et. al., 2002). The altitudes in the table span the lower two atmospheric layers and into the third atmospheric layer, the troposphere, stratosphere, and exosphere.

The troposphere, or the atmospheric layer closest to the surface, is the layer which has been reported on the most. The atmospheric pressure of this layer varies from 9 millibars at the lowest surface basin to 1 millibar at the top of Olympus Mons (25 km in altitude). Average atmospheric density on the surface of Mars is  $0.0155kg/m^3$ . Average gravity on the surface of Mars is  $3.7m/s^2$ . Each of these values decreases as the distance above the surface of Mars increases.

NASA has sent four successful rovers to Mars. NASA has also sent orbiters and unmanned stations to Mars. Together, these experiments have collected a large amount of data regarding the atmosphere on Mars.

NASA's Viking 1 and 2 missions had common goals. Both took soil samples, searched for life, took pictures of the surface, and collected general data. Each Viking, 1 and 2, had both an orbiter and a lander phase. Both of the Viking landers tested for atmospheric conditions during their descent. The next object NASA sent to land on Mars, following the Viking missions, was Pathfinder, which set up a station on Mars and carried a rover, named Sojourner. Pathfinder also tested atmospheric conditions during its descent. Magalhães, Schofield, and Seiff (1999) published the atmospheric data gathered by Pathfinder and compared it to that gathered by Viking 1. They used the new data to confirm the atmospheric data found by Viking 1. The Pathfinder data add to the Viking 1 data by finding new properties in the atmospheric layers of planet Mars.

Withers, Lorenz, and Neumann (2002) claimed that the atmospheric data from Viking 1 and Pathfinder were offset by 1–2 km in altitude. This happened because the distance above the surface of Mars was not correctly calculated perpendicular to the surface. Thus, they claim the angle skewed

all of the altitudes reported. They were able to confirm that Viking 1 and Pathfinder's results were skewed by comparing them to the data collected by MOLA (Mars Orbiter Laser Altimeter) on NASA's Mars Global Surveyor orbiter.

The last parameter to consider in the Mars atmosphere is the drag coefficient. Drag coefficient is a dimensionless quantity used to quantify the drag resistance of an object in a fluid environment. A lower drag coefficient means an object will have less aerodynamic drag. In later sections, the drag coefficient's effect on the boundary of the Biconcave Disk will be interpreted based on the numerical results.



**Figure 3.2.** A 3-Dimensional printed scale model of the Biconcave Disk.

A model of the Biconcave Disk was printed on a 3-D printer, with help from the Department of Engineering at Roger Williams University (Figure 3.2). It can be seen that the Biconcave Disk has a sharp concavity, which increases the surface area on two faces of the figure. Drag is directly related to reference area, so more area means higher drag. Drag is a component of the drag force,  $F_d$ , which is directly proportional to drag coefficient,  $C_d$ . Drag coefficient is given by the following formula:

$$C_d = \frac{2F_d}{\rho u^2 A} \quad (3.3)$$

where  $\rho$  is the mass density of the fluid,  $u$  is the flow speed of the object in the fluid, and  $A$  is the reference area, which differs from the surface area. The reference area is the portion of the surface area that is facing the flow of the fluid medium, i.e. the atmosphere. The higher the reference

area the higher the drag coefficient. Thus the shape will be less aerodynamic than a shape with a smaller reference area. The Biconcave Disk has a few different reference areas depending on how it is rotated and oriented. Thus, the effect of the drag coefficient may be maximized or minimized by rotating the Biconcave Disk for landing or taking off from planet Mars.

## 4. Numerical Methods

The Modified Galerkin method is used to numerically approximate integrals, and it is the numerical method used for this research project. There are many methods to numerically approximate an integral; the Modified Galerkin method being one of the most advanced methods.

One of the simplest methods of numerically approximating an integral is the Trapezoidal Rule. The Trapezoidal Rule divides the interval  $[a, b]$  which a definite integral is to be evaluated over into either equally spaced or non-uniformly spaced lengths. Each length has two endpoints,  $x_m$  and  $x_n$ , which correspond to values of the function,  $f$ , that is to be integrated. We will say  $f(x_m) = y_m$  and  $f(x_n) = y_n$ . Then the two points,  $(x_m, y_m)$  and  $(x_n, y_n)$ , are connected by a line segment. The line segment together with the two vertical lines at the endpoints,  $y = x_m$  and  $y = x_n$ , and the  $x$ -axis create a trapezoid. The area of a trapezoid is a well known formula, thus it is easy to calculate the area of each trapezoidal region and add the areas together. The approximate solution obtained by this method converges to the true solution as interval  $[a, b]$  is divided into smaller lengths.

For a uniform grid structure,  $(a, b)$  is divided into  $N$  equally spaced panels with the grid points  $a = x_1 < x_2 < \dots < x_{N+1} = b$ . The formula for the approximation of the integral is

$$\begin{aligned} \int_a^b f(x)dx &\approx \frac{h}{2} \sum_{k=1}^N (f(x_{k+1}) + f(x_k)) \\ &= \frac{b-a}{2N} (f(x_1) + 2f(x_2) + 2f(x_3) + \dots + 2f(x_N) + f(x_{N+1})) \end{aligned} \quad (4.1)$$

For a non-uniform grid structure, the following formula is used:

$$\int_a^b f(x)dx \approx \frac{1}{2} \sum_{k=1}^{N-1} (x_{k+1} - x_k)(f(x_{k+1}) + f(x_k)). \quad (4.2)$$

The error is calculated by subtracting the numerical result of the Trapezoidal Rule from the



value of the integral. The error is positive when the function is concave up and negative when the function is concave down, which corresponds to an under estimation or an over estimation, respectively. However, error is often evaluated as absolute error, the absolute value of the error. The Trapezoidal Rule converges to the true solution, which is to say the absolute error decreases, as the number of trapezoids  $N$  in the interval  $[a, b]$  increases. Additionally, the Trapezoidal Rule converges faster for periodic functions. The function we wish to numerically approximate is not periodic, thus we need a better methods than the Trapezoidal Rule. However, the process of breaking the interval into smaller sections to achieve a numerical approximation is an important concept.

The finite element method uses the concept of dividing the interval into smaller parts that are easier to evaluate. The finite element method allows us to move from evaluating over a two dimensional area to a three dimensional area. The area is divided into a network, or mesh of simple elements. The more elements that create the mesh, the better the approximation becomes, as the Trapezoidal Rule also demonstrated. Each element is composed of a number of nodes. Most of the nodes can move except for the nodes on the outside edge, which are the boundary conditions. The interior nodes are displaced as stress is added to them.

Each element in the finite element method is defined by an element equation. Element equations locally approximate the original partial differential equation or boundary value problem for each element of the mesh (Süli, 2012). An integral of the inner product of the residual and weight functions is created and this integral is set to equal zero. The error is minimized by fitting trial functions into the partial differential equation. The element equations are recombined into a global system of equations for final calculations, and a basis is chosen. The finite element method is a good method to use because is used to numerically approximate boundary value problems, it allows for a three-dimensional shape analysis, and any basis can be chosen (Süli, 2012). However, the finite element method is a simple case of the Galerkin Method.

## 4.1 Modified Galerkin Method

The Gaussian Quadrature method is a method for approximating integrals. It chooses points for evaluation in an optimal, rather than an equally spaced, way. The nodes  $x_1, x_2, \dots, x_n$  in the

interval  $[a, b]$  and the coefficients  $a_1, a_2, \dots, a_n$  are chosen to minimize the expected error in the approximation of the integral

$$\int_a^b f(x)dx \approx \sum_{i=1}^n a_i f(x_i). \quad (4.3)$$

For any arbitrary interval, the integral can be written in the form for the Gaussian Quadrature as

$$\int_a^b f(x)dx = \int_{-1}^1 f\left(\frac{(b-a)t + (b+a)}{2}\right)\left(\frac{b-a}{2}\right)dt. \quad (4.4)$$

Then approximated as

$$\int_{-1}^1 P(x)dx = \sum_{i=1}^n a_i P(x_i) \text{ where } a_i = \int_{-1}^1 \prod_{j=1}^n \left(\frac{x-x_j}{x_i-x_j}\right)dx. \quad (4.5)$$

The Galerkin method is a method of determining coefficients  $a_i$  of a power series solution

$$y(x) = y_0(x) + \sum_{i=1}^n a_i y_i(x) \quad (4.6)$$

of the ordinary differential equation  $L[y(x)]$ . This solution is orthogonal to every  $y_i(x)$  for  $i = 1, \dots, n$ . The goal of finding  $a_i$  is to make the residue zero for some choices of  $w(x)$ , an arbitrary weight function, for the integral

$$\int_a^b w(x)(L[y(x)] + f(x))dx = 0. \quad (4.7)$$

Where  $f(x)$  is in the vector space of  $y$ .

The Modified Galerkin method adds an infinite series to the fundamental solution of the Helmholtz equation. The infinite series removes the discontinuity that occurs as the distance from the surface of the Biconcave Disk gets very small.

The exterior boundary problem for the Neumann boundary condition is reformulated as an

integral equation of the second kind

$$u(A) = \int_S u(q) \left( \frac{e^{ikr}}{4\pi r} + \chi(A, q) \right) d\sigma_q, \quad (4.8)$$

with  $A \in D_+$ , where  $r = |A - q|$ . The kernel,  $\chi(p, q)$ , is weakly singular, which means there is a removable discontinuity that occurs as the waves radiate from close to the surface; or  $A$  tends to  $q$ . This is intuitive if one thinks about the fundamental solution,  $f(p) = \frac{e^{ikr}}{r}$ . As  $r$ , the distance from the surface of the Biconcave Disk, gets very small then  $f(p) \rightarrow \infty$ . To remove this discontinuity, we add an infinite series.

The series of radiating waves is given by

$$\chi(A, q) = ik \sum_{n=0}^{\infty} \sum_{m=-n}^n a_{nm} h_n^{(1)}(k|A|) Y_n^m \left( \frac{A}{|A|} \right) h_n^{(1)}(k|q|) \bar{Y}_n^m \left( \frac{q}{|q|} \right) \quad (4.9)$$

The Hankel functions,  $h_n^{(1)}$ , are the chosen basis vectors for the series. The Hankel functions are a linear combination of Bessel functions,  $j_n$ , and the linearly independent spherical harmonics,  $Y_n^m$ . Spherical harmonics satisfy the spherical harmonic differential equation, which is given by the angular part of Laplace's equation in spherical coordinates.  $Y_n^m(\theta, \varphi) = \sqrt{\frac{2m+1}{4\pi} \frac{(n-|m|)!}{(n+|m|)!}} p_n^{|m|}(\cos \theta) e^{im\varphi}$ ,  $n = 0, 1, 2, \dots$ ;  $m = -n, \dots, n$ ;  $p_n^{|m|}$  are the associated Legendre functions (see Appendix A).

The above series is approximated in the program by a series with a finite number of terms. There are more terms added in the interior series, so the interior is smoother than the exterior series. This means there is more continuity in the interior.

Kleinman and Roach proposed the coefficient choice for  $a_{nm}$

$$a_{nm} = -\frac{1}{2} \left( \frac{j_n(kR)}{h_n^{(1)}(kR)} + \frac{j_n'(kR)}{h_n^{(1)'}(kR)} \right) \quad (4.10)$$

for  $n = 0, 1, 2, \dots$ , and  $m = -n, \dots, n$  (1982). Kleinman and Roach also proposed that for the coefficients  $a_{nm}$  one of the following is true:

$$|2a_{nm} + 1| < 1 \text{ or} \quad (4.11)$$

$$|2a_{nm} + 1| > 1. \quad (4.12)$$

The integral equation for the Neumann condition, which can be obtained by letting  $A$  tend to a point  $p \in S$ , is

$$-2\pi\mu(p) + \int_S \mu(q) \frac{\partial}{\partial v_q} \left( \frac{e^{ikr_{qp}}}{r} - 4\pi\chi(p, q) \right) d\sigma_{dq} = -4\pi f(p) \quad (4.13)$$

The wave number  $k$ , depends on the frequency, pressure, density, and the wavelength on planet Mars for the monoharmonic waves hitting the boundary of the given surface.

From the Fredholm integral equations of the second kind, the applied Modified Galerkin method generates the following equation on the unit sphere

$$-2\hat{\mu} + \hat{K}\hat{\mu} = -4\pi\hat{f} \quad (4.14)$$

for  $\hat{f} \in C(U)$  where  $K$  is the kernel.  $L_K$  is called the integral operator, which means it is a generalization of ordinary matrix multiplication.  $K$  is a fixed measurable function on  $\mathbb{R}$ . Then the integral operator  $L_K$  with kernel  $K$  is  $L_K\mu(p) = \int K(p, q)\mu(q)dq$ .  $L_K\mu$  is defined when the integral is defined. This maps a complicated function to a less complicated domain, and the solution is mapped back to the original domain using the inverse of the integral transform. For which the solution is given by

$$\hat{\mu}_N = \sum_{j=1}^d a_j h_j \quad (4.15)$$

The program this problem is written on is Fortran 77. The subroutines for the Hankel,  $h_n^{(1)}$ , and Bessel,  $j_n$ , functions are obtained from the Newport Naval Warfare Center. The numerical computations are limited by time, processing power, and number of Galerkin coefficients available. At the highest computational level explored in the numerical results, which used 15 terms 32 interior nodes and 20 exterior nodes, the program took over one hour to compute the numerical results. The highest number of Galerkin coefficients in the program is 32 interior nodes and 20 exterior nodes. Recently, more Galerkin coefficients were found, but have not yet been added into the program because it would likely take more processing power than currently available.

## 5. Proof of Green's Theorem

Let  $S$  be a simply connected region with a piecewise smooth boundary  $C$ , oriented counter-clockwise so that  $C$  is traversed once and  $S$  is always on the left. ( $C$  given by  $r^\rightarrow(t) = p(t)\hat{i} + q(t)\hat{j}$ , where  $a \leq t \leq b$ , is simple if it does not cross itself:  $r^\rightarrow(c) \neq r^\rightarrow(d) \forall c, d \in (a, b)$ , and  $S$  is simply connected if every simple closed curve in  $S$  encloses only points that are in  $S$ .) If  $M$  and  $N$  have continuous first partial derivatives in an open region containing  $s$ , then  $\int_C Mdp + Ndq = \iint_R \left( \frac{\partial N}{\partial p} - \frac{\partial M}{\partial q} \right) dA$ .

The Bloodcell shape has continuous first partial derivatives, so Green's Theorem can be used. Green's Theorem, which states that the line integral around a boundary is equal to the double integral over the region.

**Theorem 1** *Green's Theorem: Let  $P(x, y)$  and  $Q(x, y)$  be differentiable functions defined over a region  $S$ . Let  $C$  be the piecewise smooth boundary of  $S$ . The curve  $C$  is traversed in a counterclockwise direction so that the region  $S$  is always to the left of the direction of travel. Then*

$$\oint_C (Mdp + Ndq) = \iint_S \left( \frac{\partial N}{\partial p} - \frac{\partial M}{\partial q} \right) dS \quad (5.1)$$

**Proof.** We first assume that the region  $S$  has no holes, and that the boundary  $C$  is simply connected. The curve  $C$  can then be divided into an upper and lower curve and a left and right curve. The lower edge of  $C$  can be expressed as a single valued function of  $p$ ; i.e.,  $q = f_1(p)$ . Call this the curve  $C_1$ . Likewise the upper edge of  $C$  can be expressed a single valued function of  $p$ ; i.e.,  $q = f_2(p)$ . This curve will be called  $C_2$ . The function-curve  $C_1$  runs from  $(p_1, q_1)$  to  $(p_2, q_2)$ , but  $C_2$  runs in the reverse direction from  $(p_2, Q_2)$  to  $(P_1, Q_1)$ .

Similarly horizontally simple means that the left edge of  $C$  can be expressed  $p = g_1(q)$  and the right edge as  $p = g_2(q)$ . These will be denoted as the curves  $C_3$  and  $C_4$ , respectively. The function-curve  $C_3$  runs from  $(p_3, q_3)$  to  $(p_4, q_4)$  and  $C_4$  in the reverse direction  $(p_4, q_4)$  to  $(p_3, q_3)$ .

Since the curve is oriented counter-clockwise, we have

$$\int_C M dp = \int_{C_1} M dp + \int_{C_2} M dp = \int_{p_1}^{p_2} M(p, f_1(p)) dp + \int_{p_2}^1 M(p, f_2(p)) dp.$$

$$\text{Thus } \int_C M dp = \int_{p_1}^{p_2} [M(p, f_1(p)) - M(p, f_2(p))] dp.$$

$$\text{Now consider } \iint_S \frac{\partial M}{\partial q} dq dp.$$

$$\iint_S \frac{\partial M}{\partial q} dq dp = \int_{p_1}^{p_2} \int_{f_1(p)}^{f_2(p)} \frac{\partial M}{\partial q} dq dp$$

The inner integral with respect to  $y$  can be evaluated so

$$\iint_S \frac{\partial M}{\partial q} dq dp = \int_{p_1}^{p_2} [M(p, q)]_{f_1(p)}^{f_2(p)} dp$$

and hence

$$\iint_S \frac{\partial M}{\partial q} dq dp = \int_{p_1}^{p_2} [M(p, f_2(p)) - M(p, f_1(p))] dp.$$

This expression is the negative of the expression found above.

$$\text{Therefore } \int_C M dp = - \iint_S \frac{\partial M}{\partial q} dq dp.$$

Similarly, working with the functions  $g_1$  and  $g_2$  it will be shown that

$$\int_C N dq = \iint_S \frac{\partial N}{\partial p} dp dq$$

because

$$\int_C N dq = \int_{C_3} N dq + \int_{C_4} N dq = \int_{q_3}^{q_4} N(g_2(q), q) dq + \int_{q_4}^{q_3} N(g_1(q), q) dq.$$

Thus

$$\int_C N dq = \int_{q_3}^{q_4} [N(g_2(q), q) - N(g_1(q), q)] dq.$$

Now consider

$$\iint_S \frac{\partial N}{\partial p} dp dq = \int_{q_3}^{q_4} \int_{g_1(q_3)}^{g_2(q_4)} \frac{\partial N}{\partial p} dp dq$$

Thus

$$\iint_S \frac{\partial N}{\partial p} dp dq = \int_{q_3}^{q_4} [N(g_2(q), q) - N(g_1(q), q)] dq$$

This expression is the exact expression as found above. Therefore

$$\iint_S \frac{\partial N}{\partial p} dp dq = \int_C N dq$$

The two expressions proved above are combined, through addition. It can be concluded that

$$\oint_C (M dp + N dq) = \iint_S \left( \frac{\partial N}{\partial p} - \frac{\partial M}{\partial q} \right) dS. \quad \blacksquare$$

## 6. Proof of Laplace's Equation Solution

In spherical coordinates,  $u(r, \theta, \varphi) = R(r)\Theta(\theta)\Phi(\varphi)$ , the Helmholtz Equation is given by:

$$\nabla^2 u + k^2 u = 0 \quad (6.1)$$

Laplacian  $\nabla^2 u$  is defined as

$$\nabla^2 u = \frac{\partial^2 u}{\partial r^2} + \frac{2}{r} \frac{\partial u}{\partial r} + \frac{1}{r^2 \sin^2(\theta)} \frac{\partial^2 u}{\partial \varphi^2} + \frac{1}{r^2} \frac{\partial^2 u}{\partial \theta^2} + \frac{\cot(\theta)}{r^2} \frac{\partial u}{\partial \theta} \quad (6.2)$$

substituting this into the Helmholtz Equation, we get:

$$\frac{\partial^2 u}{\partial r^2} + \frac{2}{r} \frac{\partial u}{\partial r} + \frac{1}{r^2 \sin^2(\theta)} \frac{\partial^2 u}{\partial \varphi^2} + \frac{1}{r^2} \frac{\partial^2 u}{\partial \theta^2} + \frac{\cot(\theta)}{r^2} \frac{\partial u}{\partial \theta} + k^2 u = 0$$

Then, we can begin simplifying

$$r^2 \cdot \left[ \frac{\partial^2 u}{\partial r^2} + \frac{2}{r} \frac{\partial u}{\partial r} + \frac{1}{r^2 \sin^2(\theta)} \frac{\partial^2 u}{\partial \varphi^2} + \frac{1}{r^2} \frac{\partial^2 u}{\partial \theta^2} + \frac{\cot(\theta)}{r^2} \frac{\partial u}{\partial \theta} + k^2 u = 0 \right]$$

$$r^2 \frac{\partial^2 u}{\partial r^2} + 2r \frac{\partial u}{\partial r} + \frac{1}{\sin^2(\theta)} \frac{\partial^2 u}{\partial \varphi^2} + \frac{\partial^2 u}{\partial \theta^2} + \cot(\theta) \frac{\partial u}{\partial \theta} + r^2 k^2 u = 0$$

We need to find the first and second partial derivatives for  $u$  with respect to  $r, \theta$ , and  $\varphi$ . To simplify the equations a bit, I change to Lagrange's Notation.

$$u(r, \theta, \varphi) = R(r)\Theta(\theta)\Phi(\varphi) \rightarrow \frac{\partial u}{\partial r} = \Theta\Phi R', \frac{\partial^2 u}{\partial r^2} = \Theta\Phi R'', \dots$$

Now, we can substitute the derivatives into the Helmholtz Equation and simplify to begin to separate all of the variables.

$$\begin{aligned} r^2 \frac{\partial^2 u}{\partial r^2} + 2r \frac{\partial u}{\partial r} + r^2 k^2 u + \frac{1}{\sin^2(\theta)} \frac{\partial^2 u}{\partial \varphi^2} + \frac{\partial^2 u}{\partial \theta^2} + \cot(\theta) \frac{\partial u}{\partial \theta} &= 0 \\ [r^2 \Theta \Phi R'' + 2r \Theta \Phi R' + r^2 k^2 \Theta \Phi R + \frac{1}{\sin^2(\theta)} \Theta \Phi'' R + \Theta'' \Phi R + \cot(\theta) \Theta' \Phi R = 0] / (\Theta \Phi R) \\ \frac{r^2 R'' + 2r R' + r^2 k^2 R}{R} + \frac{1}{\sin^2(\theta)} \frac{\Phi''}{\Phi} + \frac{\Theta'' + \cot(\theta) \Theta'}{\Theta} &= 0 \end{aligned}$$

To make these separable equations of a single-variable, I will introduce the first separation constant,  $\lambda_1$ . I can do this because I made  $R(r)$  independent of  $\Theta(\theta)$  and  $\Phi(\varphi)$ . This allows me

to separate the equation involving  $R(r)$  from those of phi and theta.

$$\frac{r^2 R'' + 2rR' + r^2 k^2 R}{R} = -\frac{1}{\sin^2(\theta)} \frac{\Phi''}{\Phi} - \frac{\Theta'' + \cot(\theta)\Theta'}{\Theta} = \lambda_1$$

To set up the radial dependence equation, we use the equation found in the previous step and the information that  $\lambda_1 = n(n+1)$ .

$$\frac{r^2 R'' + 2rR' + r^2 k^2 R}{R} = \lambda_1; \lambda_1 = n(n+1)$$

$$\left[ \frac{r^2 R'' + 2rR' + r^2 k^2 R}{R} = n(n+1) \right] R$$

$$r^2 R'' + 2rR' + r^2 k^2 R = n(n+1)R$$

$$r^2 R'' + 2rR' + r^2 k^2 R - n(n+1)R = 0$$

So the equation for radial dependence is:

$$r^2 R'' + 2rR' + [r^2 k^2 - n(n+1)]R = 0.$$

I now use the second part of the equation found before (a.) to set up the separated equations for  $\Theta(\theta)$  and  $\Phi(\varphi)$ .

$$-\frac{1}{\sin^2(\theta)} \frac{\Phi''}{\Phi} - \frac{\Theta'' + \cot(\theta)\Theta'}{\Theta} = \lambda_1$$

First, I must isolate all  $\Theta(\theta)$  from  $\Phi(\varphi)$  so these functions will be completely independent of one another.

$$\begin{aligned} \sin^2(\theta) \left[ -\frac{1}{\sin^2(\theta)} \frac{\Phi''}{\Phi} - \frac{\Theta'' + \cot(\theta)\Theta'}{\Theta} \right] &= \lambda_1 \\ -\frac{\Phi''}{\Phi} - \sin^2(\theta) \cdot \left( \frac{\Theta'' + \cot(\theta)\Theta'}{\Theta} \right) &= \sin^2(\theta)\lambda_1 \\ -\frac{\Phi''}{\Phi} - \sin^2(\theta) \cdot \left( \frac{\Theta'' + \cot(\theta)\Theta'}{\Theta} + \lambda_1 \right) &= 0 \end{aligned}$$

Now, I introduce the second separation constant,  $\lambda_2$ , to separate the two resulting differentiation equations. We know this constant to be  $\lambda_2 = m^2$ .

$$-\frac{\Phi''}{\Phi} = \sin^2(\theta) \cdot \left( \frac{\Theta'' + \cot(\theta)\Theta'}{\Theta} + \lambda_1 \right) = \lambda_2; \lambda_2 = m^2$$

Solving for  $\Phi(\varphi)$ , we find:

$$\begin{aligned} -\frac{\Phi''}{\Phi} &= m^2 \\ \left[ -\frac{\Phi''}{\Phi} = m^2 \right] \cdot \Phi & \\ -\Phi'' &= m^2 \Phi \\ -\Phi'' - m^2 \Phi &= 0 \\ \Phi'' + m^2 \Phi &= 0 \end{aligned}$$

Using the second half of the equation above to solve  $\Theta(\theta)$ :



$$\sin^2(\theta) \cdot \left( \frac{\Theta'' + \cot(\theta)\Theta'}{\Theta} + \lambda_1 \right) = \lambda_2$$

$$\frac{\Theta'' + \cot(\theta)\Theta'}{\Theta} + \lambda_1 = \frac{\lambda_2}{\sin^2(\theta)}$$

$$\frac{\Theta'' + \cot(\theta)\Theta'}{\Theta} + n(n+1) = \frac{m^2}{\sin^2(\theta)}$$

$$\Theta \left( \frac{\Theta'' + \cot(\theta)\Theta'}{\Theta} + n(n+1) \right) = \Theta \cdot \left( \frac{m^2}{\sin^2(\theta)} \right)$$

$$\Theta'' + \cot(\theta)\Theta' + \Theta n(n+1) = \Theta \cdot \left( \frac{m^2}{\sin^2(\theta)} \right)$$

$$\Theta'' + \cot(\theta)\Theta' = \Theta \cdot \left( \frac{m^2}{\sin^2(\theta)} \right) - \Theta n(n+1)$$

$$\Theta'' + \cot(\theta)\Theta' = \Theta \cdot \left( \left( \frac{m^2}{\sin^2(\theta)} \right) - n(n+1) \right)$$

$$\Theta'' + \cot(\theta)\Theta' - \Theta \cdot \left( \left( \frac{m^2}{\sin^2(\theta)} \right) - n(n+1) \right) = 0$$

$$\Theta'' + \cot(\theta)\Theta' + \Theta \cdot \left( n(n+1) - \left( \frac{m^2}{\sin^2(\theta)} \right) \right) = 0$$

We now can use the substitution  $x = \cos(\theta)$  to begin changing the differential equation back to cartesian coordinates.

$$\text{Since } x = \cos(\theta), \theta = \cos^{-1}(x)$$

$$\frac{dx}{d\theta} = -\sin(\theta)$$

$$\frac{d^2x}{d\theta^2} = -\cos(\theta)$$

$$\frac{dx}{d\theta} = -\frac{1}{\sqrt{1-x^2}}$$

$$\frac{d^2\theta}{dx^2} = -x \cdot (1-x^2)^{-3/2}$$

$$\frac{d^2\Theta}{d\theta^2} + \cot(\theta) \frac{d\Theta}{d\theta} + \Theta \cdot \left[ n(n+1) - \left( \frac{m^2}{\sin^2(\theta)} \right) \right] = 0$$

$$\frac{d^2\Theta}{d\theta^2} + \cot(\theta) \frac{d\Theta}{d\theta} + \Theta \cdot \left[ n(n+1) - \left( \frac{m^2}{\sin^2(\theta)} \right) \right] = 0$$

$$\frac{d^2\Theta}{\left[ -\frac{1}{\sqrt{1-x^2}} dx \right]^2} + \cot(\cos^{-1}(x)) \frac{d\Theta}{-(1-x^2)^{-1/2} dx} + \Theta \cdot \left[ n(n+1) - \left( \frac{m^2}{\sin^2(\cos^{-1}(x))} \right) \right] = 0$$

$$(1-x^2) \frac{d^2\Theta}{dx^2} + \frac{x}{(1-x^2)^{1/2}} \cdot -(1-x^2)^{1/2} \cdot \frac{d\Theta}{dx} + \Theta \cdot \left[ n(n+1) - \left( \frac{m^2}{1-x^2} \right) \right] = 0$$

$$-\frac{(1-x^2)^{3/2}}{x} \frac{d^2\Theta}{dx^2} - 2x \frac{d\Theta}{dx} + \Theta \cdot \left[ n(n+1) - \left( \frac{m^2}{1-x^2} \right) \right] = 0$$

## 7. Numerical Results

This project involved finding the best convergence results for the Biconcave Disk shape. The shape and calculations were adjusted to fit conditions on planet Mars. Real wavenumbers,  $k$ , that occur in the atmosphere of planet Mars have been calculated in Section 3. The radius of the Biconcave Disk was initially approximated by using a constant radius of 1 (a sphere). Then the radius of the Biconcave Disk was then approximated by the radius of an ellipsoid (Equation 3.9). Both approximations of the radius gave the same convergence results, so the radius of the ellipsoid was used to compute the numerical results reported in this section because the ellipsoid provided a closer approximate radius than the sphere. The following equations were used for the boundary of the Biconcave Disk:

$$x = A \sin(\varphi) \cos(\theta)$$

$$y = B \sin(\varphi) \sin(\theta) \tag{7.1}$$

$$z = C \left( \left( 1 - \frac{\lambda}{2} \right) + \frac{\lambda}{2} \sin(\varphi) \right) \cos(\varphi)$$

The coefficients  $A$ ,  $B$ ,  $C$ , and  $\lambda$  were determined first in the computations. The coefficients  $A$  and  $B$  were kept at 1 because these coefficients determine a stretch or shrink along the x- and y-axis, respectively. Using  $A = B = 1$  creates a circular cross section on the xy-plane, instead of the elliptic cross section created by changing only one of  $A$  or  $B$ . The circular shape was preferred because it was consistent with the shape of a blood cell. Figure 7.1 shows how the z-coordinate changes when  $C$  is changed. From Figure 7.1 it was determined that when  $C = 1$  the Biconcave

Disk is very tall, but as  $C$  decreases, the shape flattens.

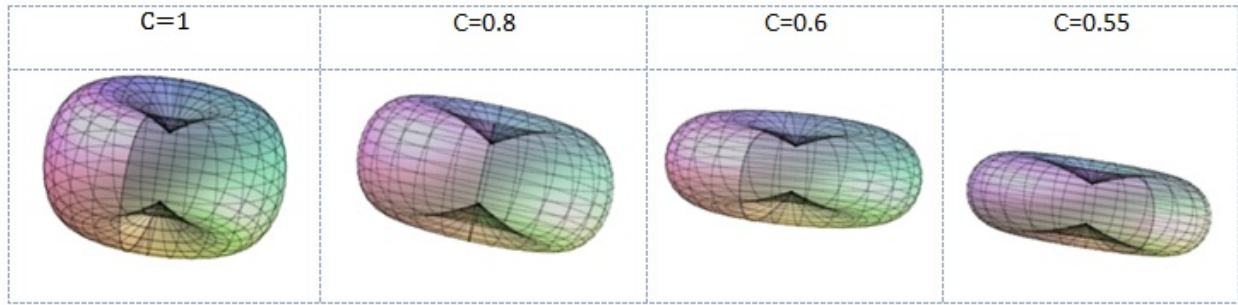


**Figure 7.1.** A few figures to demonstrate how the Biconcave Disk morphs as  $C$  decreases.

One can see that as the value of  $C$  decreases, the bloodcell shape becomes flatter and the concave sides get closer toward the center. The ideal shape is a compromise between the shape being relatively flat yet not too flat that the concave sides touch in the center. The chosen value for  $C$  should also maintain good convergence results because it was determined that when  $C = 1$  the approximation is good (Table 2.1). Thus, the convergence was determined for decreasing values of  $C$  (Table 7.1). Table 7.1 shows the preliminary results evaluated for the Modified Galerkin Method over the surface of the Biconcave Disk for the Neumann boundary condition.

Point Coordination	Absolute Error for Coefficient of z-coordinate			
	$C = 1$	$C = 0.8$	$C = 0.6$	$C = 0.55$
(1, 2, 3000)	$1.365D - 06$	$4.559D - 06$	$9.213D - 06$	$1.141D - 05$
(1, 2000, 3000)	$1.136D - 06$	$3.794D - 06$	$7.665D - 06$	$9.498D - 06$
(1000, 2000, 3000)	$1.094D - 06$	$3.656D - 06$	$7.387D - 06$	$9.152D - 06$
(11, 12, 13)	$3.729D - 04$	$6.566D - 04$	$1.327D - 03$	$1.644D - 03$

**Table 7.1.** Comparing convergence results for the Neumann boundary conditions for the Biconcave Disk for various values of  $C$ , the coefficient of the  $z$ -coordinate. We approximate with a radius of 1,  $N = 5; k = 0.001; \lambda = 0.4$ ; number of interior nodes was 16; number of exterior nodes was 16. The boundary function was  $f_1(p)$ . As the value of  $C$  decreases, the absolute error increases.

Various possible values of  $C$  were tested to determine which  $C$  value should be used for further computations (Table 7.1). The results were fairly good for all values tested. The absolute error increased as the value of  $C$  decreased. It was deduced from Table 7.1 that the value for the  $z$ -coefficient that should be used is  $C = 0.55$ . This value produces a shape that is flatter than the shape when  $C = 1$ , yet the concave sides do not touch in the center, and the the absolute error is low enough to be a viable shape for use in the design of a spacecraft to one day land on planet Mars.

The results in Table 7.1 were evaluated at a low computational level, so the error approximation will likely improve as the number of terms increase, the number of nodes increase, and the other conditions are changed.

The  $z$ -coordinate coefficient  $C = 0.55$  was chosen because it creates a shape which is closest to the shape of a “Bloodcell” while maintaining a good convergence (Table 3 and Figure 2).

There is no change in absolute error as  $N$ , the number of terms in the infinite series, increases (Table 4); however, I will keep computing using 15 terms,  $N = 0, 15$ , because this eliminates more interior Dirichlet eigenvalues for the Biconcave Disk. This result will be useful in further computations.

Point Coordination	Absolute Error for Low Wavenumbers			
	k=0.052278	k=0.065348	k=0.07847	k=0.091487
(1,2,3000)	2.921D-06	2.920D-06	2.919D-06	2.918D-06
(1,2000,3000)	2.430D-06	2.430D-06	2.429D-06	2.428D-06
(1000,2000,30000)	2.342D-06	2.341D-06	2.340D-06	2.340D-06
(11,12,13)	4.206D-04	4.205D-04	4.204D-04	4.202D-04

**Table 7.2.** Comparing convergence results for various wavenumbers,  $k$ -values, using the Neumann boundary conditions for the Biconcave Disk. We approximated with a Radius of 1, number of interior nodes was 32, the number of exterior nodes was 16,  $\lambda = 1.4$ ;  $A = 1$ ,  $B = 1$ ,  $C = 0.55$ ,  $N = 15$ . The boundary function was  $f_1(p)$ . Better convergence results were obtained as the  $k$ -value increased.

The atmospheric conditions on Planet Mars tend to produce very small wave numbers as a result of the low frequencies that arise in the atmosphere. Dinh (2015) calculated a range of wavenumbers on planet Mars between  $k = 0.05$  and  $k = 0.1$ . In Table 7.2., his calculated wavenumbers are tested on The Biconcave Disk. These wavenumbers give better convergence results as the wavenumbers increase. The wavenumbers that Dinh (2015) calculated are very low and correspond to low frequencies in the atmosphere. These waves likely originate in the outermost atmospheric layers of planet Mars. The mesosphere into the exosphere of planet Mars have conditions that produce low wavenumbers such as the ones tested in Table 7.2. These wavenumbers correspond to low frequencies which occur as the atmosphere gets thinner and waves travel more slowly. Thus, a value such as  $k = 0.052278$  may be produced in an elevation around 200 km above the surface of Mars. The wavenumber 0.091487 may be produced around 160 km above the surface of Mars. The Mars atmosphere is more dense with gasses at 160 km altitude than at 200 km, so the waves can travel

at a higher frequency. Higher frequencies correlate to higher wavenumbers.

The wavenumbers that were calculated in Section 3 range from  $k = 0.13963$  and  $k = 0.31416$ . These wavenumbers are produced in the lower two atmospheric layers and through the break between the second and third layers. It is good that as wavenumbers increase the convergence results get better for the outer layers because this suggests that when the wavenumbers between  $k = 0.13963$  and  $k = 0.31416$  are tested, the convergence results may be as good as or possibly better than the convergence results for the outer layers.

In the following subsections, the computations will be refined to produce the best convergence results for the Biconcave Disk. The best convergence results will be calculated for various possible boundary functions and then the results for each boundary function will be compared against each other.

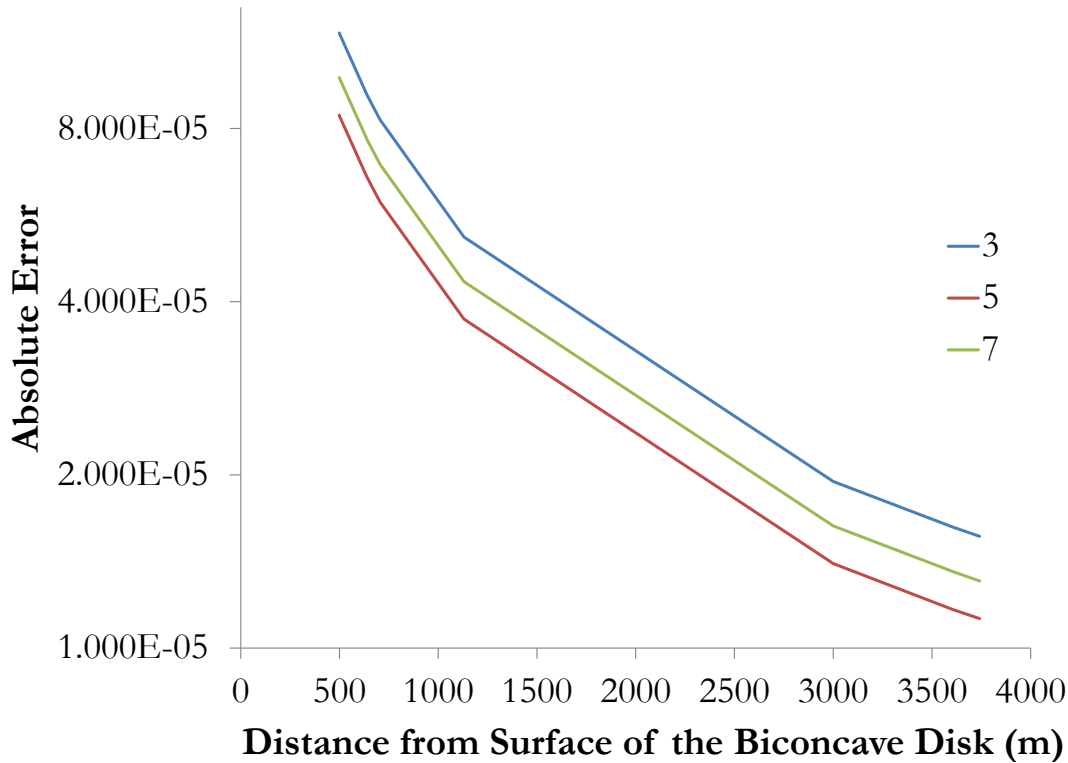
## 7.1 Convergence Results:

### Boundary Function One

Distance from the Surface of the Biconcave Disk (m)	Absolute Error for Degree of the Boundary Function for an Ellipsoidal Radius		
	3	5	7
104	$5.584D - 04$	$4.017D - 04$	$4.671D - 04$
190	$3.066D - 04$	$2.206D - 04$	$2.565D - 04$
499	$1.173D - 04$	$8.439D - 05$	$9.812D - 05$
500	$1.169D - 04$	$8.409D - 05$	$9.780D - 05$
639	$9.160D - 05$	$6.590D - 05$	$7.662D - 05$
640	$9.141D - 05$	$6.576D - 05$	$7.646D - 05$
706	$8.280D - 05$	$5.957D - 05$	$6.927D - 05$
3,000	$1.948D - 05$	$1.402D - 05$	$1.630D - 05$
3,606	$1.623D - 05$	$1.167D - 05$	$1.358D - 05$
3,742	$1.564D - 05$	$1.125D - 05$	$1.308D - 05$
1,130	$5.184D - 05$	$3.730D - 05$	$4.336E - 05$

**Table 7.3.**  $N = 0, 15$  terms, 16 interior nodes, 8 exterior nodes, and  $A = 1, B = 1, C = 0.55, \lambda = 1.4, k = 0.13963$ , the boundary function  $f_1(p)$  are used. Change in absolute error as the distance from the surface of the Biconcave Disk increases for different degrees of the boundary function. Degree= 5 gives the best convergence results, thus we can conclude that degree of 7 is an over approximation and 3 is an under approximation.

When the degree of the boundary function is 5, the absolute error is minimized (Table 7.3). Thus, we conclude that when the degree of the boundary function is 7, this is an over approximation. Similarly, when the degree of the boundary function is 3, this produces an under approximation. So, a degree of 5 is kept for further computations that use boundary function 1.



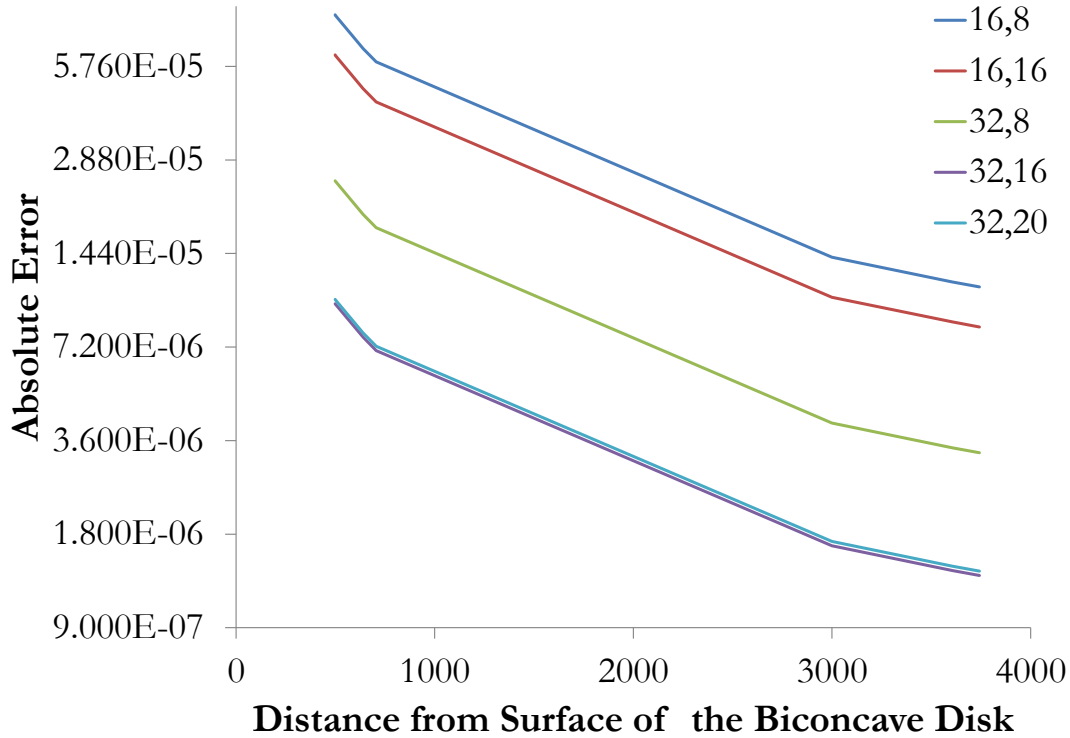
**Graph 7.1.**  $N = 0, 15$  terms, 16 exterior nodes, 8 interior nodes, and  $A = 1, B = 1, C = 0.55, \lambda = 1.4, k = 0.13963, f_1(p)$  were used. Change in absolute error as the distance from the surface of the Biconcave Disk increases for different degrees of the boundary function. The convergence results get closer to zero as the distance from the Biconcave Disk increases.

We see in Graph 7.1 (which corresponds to table 7.3) that when the degree of the boundary function is 5, the best approximation is achieved. It is also seen that the error decreases as the wave's distance from the surface increases. The solutions are only evaluated up to 4,000 meters (4 km) even though the thickness of the atmosphere on planet Mars is about 200 km. The waves that radiate from a distance further than 4,000 meters from the surface of the Biconcave Disk will continue to produce even better convergence results as the distance from the Biconcave Disk increases. Thus, 4,000 meters from the surface of the Biconcave Disk is the largest distance evaluated in the current results.

Distance from the Surface of the Biconcave Disk (m)	Absolute Error for Interior and Exterior Nodes for an Ellipsoidal Radius			
	16, 8	16, 16	32, 16	32, 20
499	$8.439D - 05$	$6.271D - 05$	$9.928D - 06$	$1.025D - 05$
500	$8.409D - 05$	$6.249D - 05$	$9.905D - 06$	$1.023D - 05$
639	$6.590D - 05$	$4.897D - 05$	$7.752D - 06$	$8.004D - 06$
640	$6.576D - 05$	$4.886D - 05$	$7.742D - 06$	$7.993D - 06$
640	$6.581D - 05$	$4.890D - 05$	$7.745D - 06$	$7.997D - 06$
706	$5.957D - 05$	$4.426D - 05$	$7.012D - 06$	$7.240D - 06$
1,130	$3.730D - 05$	$2.771D - 05$	$4.388D - 06$	$4.530D - 06$
3,000	$1.402D - 05$	$1.041D - 05$	$1.651D - 06$	$1.705D - 06$
3,606	$1.167D - 05$	$8.675D - 06$	$1.375D - 06$	$1.419D - 06$
3,742	$1.125D - 05$	$8.361D - 06$	$1.325D - 06$	$1.368D - 06$

**Table 7.4.**  $N = 0, 15$  terms, Degree of the boundary function is 5,  $A = 1$ ,  $B = 1$ ,  $C = 0.55$ ,  $\lambda = 1.4$ ,  $k = 0.13963$ ,  $f_1(p)$  were used. The number of interior nodes varies from 16 to 32, and the number of exterior nodes varies from 16 to 20. In general, the absolute error decreases as distance increases. 32 interior and 16 exterior nodes gives the best convergence results.

A greater number of nodes tends to give better convergence results (Table 7.4). The Modified Galerkin Method is a numerical method for approximating the kernel of the Fredholm integral equation, thus a greater number of nodes should produce a better approximation of the kernel. The results in Table 7.4 support this method. The best convergence results are observed for the node combination of 32 interior nodes and 16 exterior nodes. As the number of interior nodes increases from 16 to 32, the convergence results improve. As the number of exterior nodes increases from 8 to 16, the convergence results also improve. However, when the number of exterior nodes is 16 better convergence results are obtained than when the number of exterior nodes is 20. This occurs because 20 exterior nodes is an over estimation. For other computations using boundary function 1, 32 interior and 16 exterior nodes will continue to be used.



**Graph 7.2.**  $N = 0, 15$  terms, degree of the boundary function is 5,  $A = 1$ ,  $B = 1$ ,  $C = 0.55$ ,  $\lambda = 1.4$ ,  $k = 0.13963$ ,  $f_1(p)$  were used. The number of interior nodes varies from 16 to 32, and the number of exterior nodes varies from 8 to 20. Change in absolute error as the distance from the surface of the Biconcave Disk increases for different number of terms added. In general, the absolute error decreases as distance increases. 32, 16 gives the best convergence results.

It can be seen in Graph 7.2 (corresponding to table 7.4) that the best approximation arises from the node combination of 32 interior and 16 exterior nodes. The approximation is only slightly better than 32 interior and 20 exterior nodes. Given a wider range of Galerkin coefficients, it could be determined whether the absolute error would get better or worse if the nodes kept increasing. It was seen that the convergence results improved from 16 to 32 interior nodes, so perhaps given 64 interior nodes the convergence results would improve even more. With a greater number of interior nodes, the number of exterior nodes could possibly also increase and improve convergence results. So, given the Galerkin coefficients for this many nodes, it could be determined whether increasing the node combination from 32, 20 to say 64, 20 or 64, 32 would provide better convergence results. However, the computational limit is 32, 20 in the current program. So, we must assume that 20 exterior nodes is an over approximation.

Between Graphs 7.1 and 7.2, we see a consistently decreasing in convergence. As each level



of computation is built upon the previous level. the best possible conditions for the problem are combined and the numerical results keep improving. Where in Graph 7.1, the best convergence was E-05, in figure 7.3 the best convergence is close to E-07.

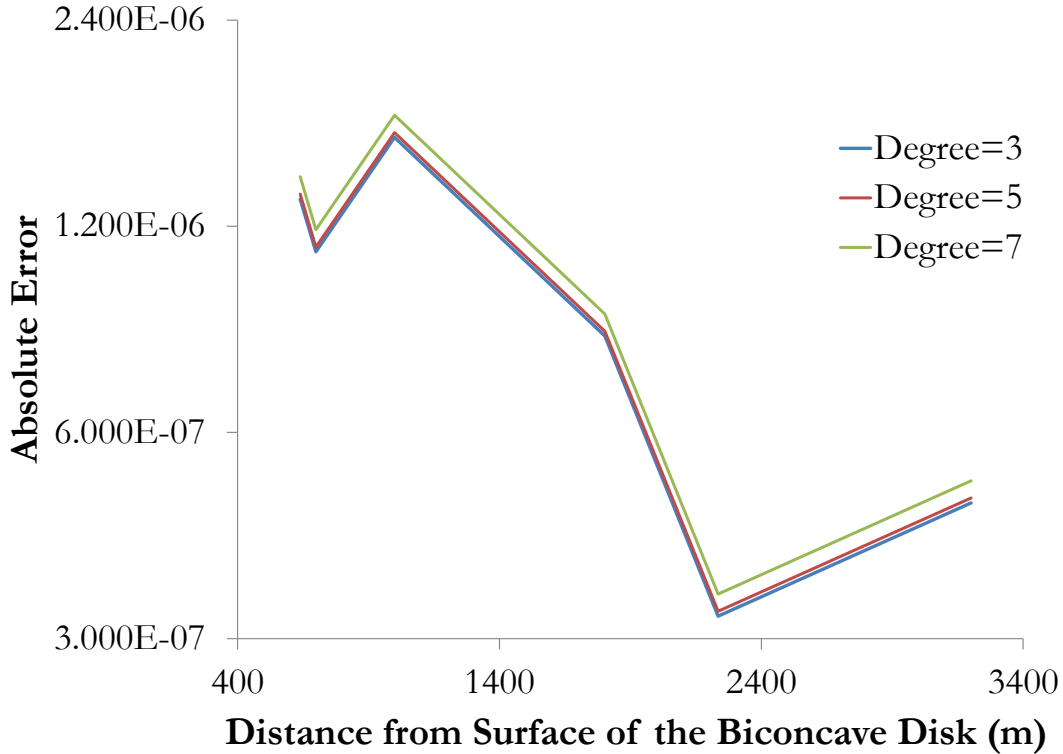
## 7.2 Convergence Results:

### Boundary Function Two

Distance from the Surface of the Biconcave Disk (m)	Absolute Error for Degree of the Boundary Function for an Ellipsoidal Radius		
	3	5	7
499	4.315D - 06	4.385D - 06	4.647D - 06
499	4.315D - 06	4.385D - 06	4.647D - 06
500	1.079D - 03	1.097D - 03	1.162D - 03
639	1.314D - 06	1.337D - 06	1.417D - 06
640	6.579D - 04	6.685D - 04	7.086D - 04
640	5.263D - 04	5.348D - 04	5.668D - 04
706	5.394D - 04	5.482D - 04	5.810D - 04
3,000	1.798D - 04	1.837D - 04	1.973D - 04
3,606	1.245D - 04	1.265D - 04	1.341D - 04
3,742	1.156D - 04	1.175D - 04	1.245D - 04

**Table 7.5.**  $N = 0, 15$  terms, 16 interior nodes, 8 exterior nodes, and  $A = 1, B = 1, C = 0.55, \lambda = 1.4, k = 0.13963, f_2(p)$  were used. Change in absolute error as the distance from the surface of the Biconcave Disk increases for different degrees of the boundary function. *Degree = 3* gives the best convergence results, thus we can conclude that when the degree of the boundary function is 7 or 5, it is an over approximation. The best point (highlighted in green) is due to the fact this point is near the smooth portion. Likewise the point highlighted in yellow gives smaller convergence results because the wave at this point radiates toward the “dip.”

For boundary function 2, when the degree of the boundary function is 3 the best convergence results are obtained (Table 7.5). Therefore, when the degree of the boundary function is either 5 or 7 it is an over approximation. It is possible that using a degree of 3 will simplify the computation too much which means degree 3 produces a better result by leaving data out, so the degree of 5 will be used for further computations with boundary function 2. Graph 7.3 shows that the convergence results for degree 5 are very close to the convergence results for degree 3 of the boundary function. Therefore, it is reasonable to use degree 5 instead of degree 3.



**Graph 7.3.**  $N = 0, 15$  terms, 16 interior nodes, 8 exterior nodes, and  $A = 1$ ,  $B = 1$ ,  $C = 0.55$ ,  $\lambda = 1.4$ ,  $k = 0.13963$ ,  $f_2(p)$  were used. Change in absolute error as the distance from the surface of the Biconcave Disk increases for different degrees of the boundary function. Generally, the convergence gets closer to 0 as the distance from the Biconcave Disk increases. Degree=3 gives the best convergence results, thus we can conclude that degree of 7 or 5 is an over approximation.

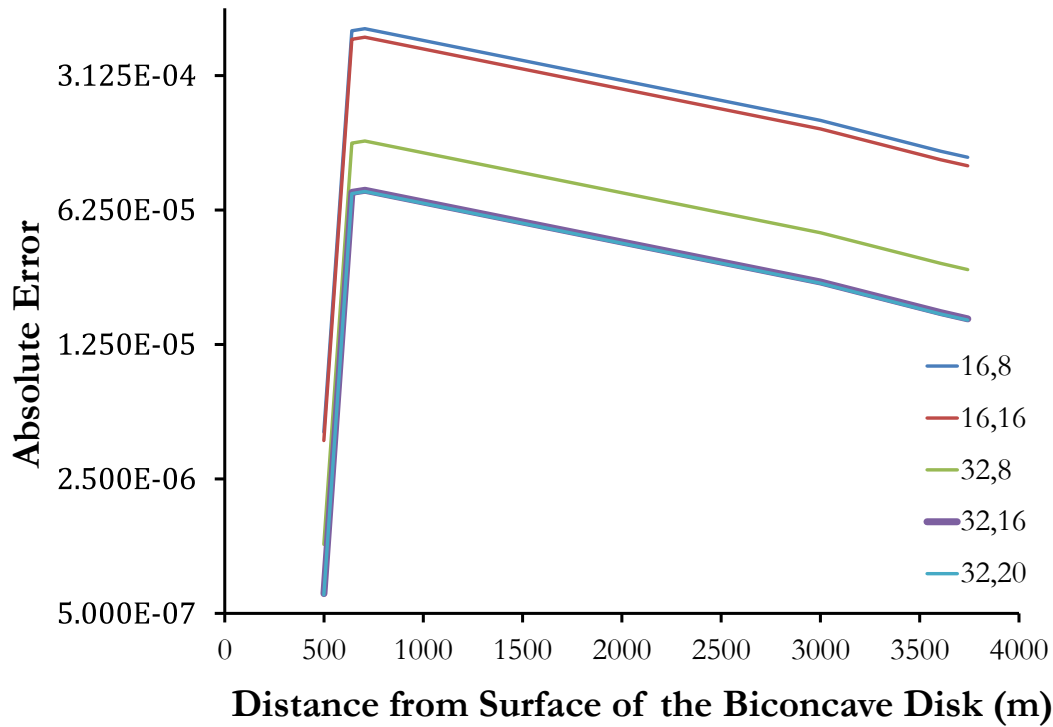
Graph 7.3 (corresponding to Table 7.5) displays that when the degree of the boundary function is 3, the best convergence results are obtained. It can also be seen that when the degree of the boundary function is 5, the convergence results are comparable to degree of 3. Thus, the degree of the boundary function will be 5 for further computations using boundary function 2.

It may be noted that the graph does not exhibit the steady decreases in error as the distance from the surface of the Biconcave Disk increases, as was seen with boundary function 1. This is because the convergence results for boundary function 2 are dependent on the orientation of the incoming wave. If the wave radiates toward the depression in the top or bottom of the bloodcell, the convergence results are significantly worse. Likewise, if the wave radiates toward the smooth, sphere-like portion of the bloodcell, the convergence results improve. Note that distance 639 meters and 640 meters, seemingly close numbers, have drastically different absolute error results (Table 7.5).

Distance from the Surface of the Biconcave Disk (m)	Absolute Error for Interior and Exterior Nodes for an Ellipsoidal Radius			
	16, 8	16, 16	32, 16	32, 20
499	$4.385D - 06$	$3.959D - 06$	$6.339D - 07$	$6.243D - 07$
499	$4.385D - 06$	$3.959D - 06$	$6.339D - 07$	$6.243D - 07$
500	$1.097D - 03$	$9.901D - 04$	$1.586D - 04$	$1.562D - 04$
639	$1.337D - 06$	$1.207D - 06$	$1.933D - 07$	$1.903D - 07$
640	$6.685D - 04$	$6.036D - 04$	$9.669D - 05$	$9.522D - 05$
640	$5.348D - 04$	$4.829D - 04$	$7.928D - 05$	$7.807D - 05$
706	$5.482D - 04$	$4.949D - 04$	$7.928D - 05$	$7.807D - 05$
3,000	$1.827D - 04$	$1.650D - 04$	$2.644D - 05$	$2.604D - 05$
3,606	$1.265D - 04$	$1.142D - 04$	$1.830D - 05$	$1.802D - 05$
3,742	$1.175D - 04$	$1.061D - 04$	$1.699D - 05$	$1.673D - 05$

**Table 7.6.**  $N = 0, 15$  terms, degree of the boundary function is 5,  $A = 1$ ,  $B = 1$ ,  $C = 0.55$ ,  $\lambda = 1.4$ ,  $k = 0.13963$ ,  $f_2(p)$  were used. The number of interior nodes varies from 16 to 32, and the number of exterior nodes varies from 8 to 20. In general, the absolute error decreases as number of nodes increases. 32 interior and 20 exterior nodes gives the best convergence results. The best point on the graph (highlighted in green) is near the smooth part of the Bloodcell. The point highlighted in yellow gives smaller convergence results because the wave originating from this point radiates toward the “dip.”

It is seen from Table 7.6 that the best approximation is obtained when the number of interior nodes is 32 and number of exterior nodes is 20. as the number of interior nodes increased from 16 to 32, the convergence results improved. This suggests that a greater number of interior nodes will produce a better approximation. When the number of exterior nodes increased from 8 to 16, the convergence results improved. Also, when the number of exterior nodes increased from 16 to 20, the convergence results improved. However, the increase from 16 to 20 exterior nodes did not produce as much of a difference as from 8 to 16 interior nodes. This suggests that more than 20 exterior nodes will be an over approximation. Given a wider range of galerkin coefficients, this hypothesis could be tested by examining the difference of convergence results between the node combinations 32, 20, 64, 20, and 64, 32. Any node combination of the infinite series less than 32, 20 is an under approximation. The combination of 32 interior and 20 exterior nodes will be used in further calculations for boundary function 2.



**Graph 7.4.**  $N = 0,15$  terms, degree of the boundary function is 5,  $A = 1$ ,  $B = 1$ ,  $C = 0.55$ ,  $\lambda = 1.4$ ,  $k = 0.13963$ ,  $f_2(p)$  were used. The number of interior nodes varies from 16 to 32, and the number of exterior nodes varies from 8 to 20. In general, the absolute error decreases as distance increases. 32,16 gives the best convergence results. Change in absolute error as the distance from the surface of the Biconcave Disk increases for different amounts of nodes added.

It is clear that as the number of interior and exterior nodes increase, the absolute error decreases (Graph 7.4). 32 interior and 20 exterior nodes is slightly better than 32 interior and 16 exterior nodes. This data suggests that a higher number of interior and exterior nodes produces better convergence results. The node combination of 32 interior and 20 exterior nodes will be used for further calculations using boundary function 2. Again, a steep spike is displayed in the graph, which is due to the different orientations of the incoming waves.

Distance from the Surface of the Biconcave Disk (m)	Absolute Error for Various Wavenumbers for an Ellipsoidal Radius			
	$k = 0.13963$	$k = 0.18480$	$k = 0.26180$	$k = 0.31416$
190	$2.568D - 04$	$2.576D - 04$	$2.596D - 04$	$2.613D - 04$
499	$6.243D - 07$	$6.262D - 07$	$6.306D - 07$	$6.345D - 07$
499	$6.243D - 07$	$6.262D - 07$	$6.306D - 07$	$6.345D - 07$
639	$1.903D - 07$	$1.909D - 07$	$1.923D - 07$	$1.934D - 07$
640	$9.522D - 05$	$9.556D - 05$	$9.635D - 05$	$9.704D - 05$
706	$7.807D - 05$	$7.834D - 05$	$7.897D - 05$	$7.952D - 05$
3,000	$2.604D - 05$	$2.614D - 05$	$2.637D - 05$	$2.658D - 05$
3,606	$1.802D - 05$	$1.808D - 05$	$1.824D - 05$	$1.837D - 05$
3,742	$1.673D - 05$	$1.679D - 05$	$1.693D - 05$	$1.705D - 05$
5.4	$1.532D - 08$	$1.154D - 08$	$8.093D - 08$	$6.706D - 08$

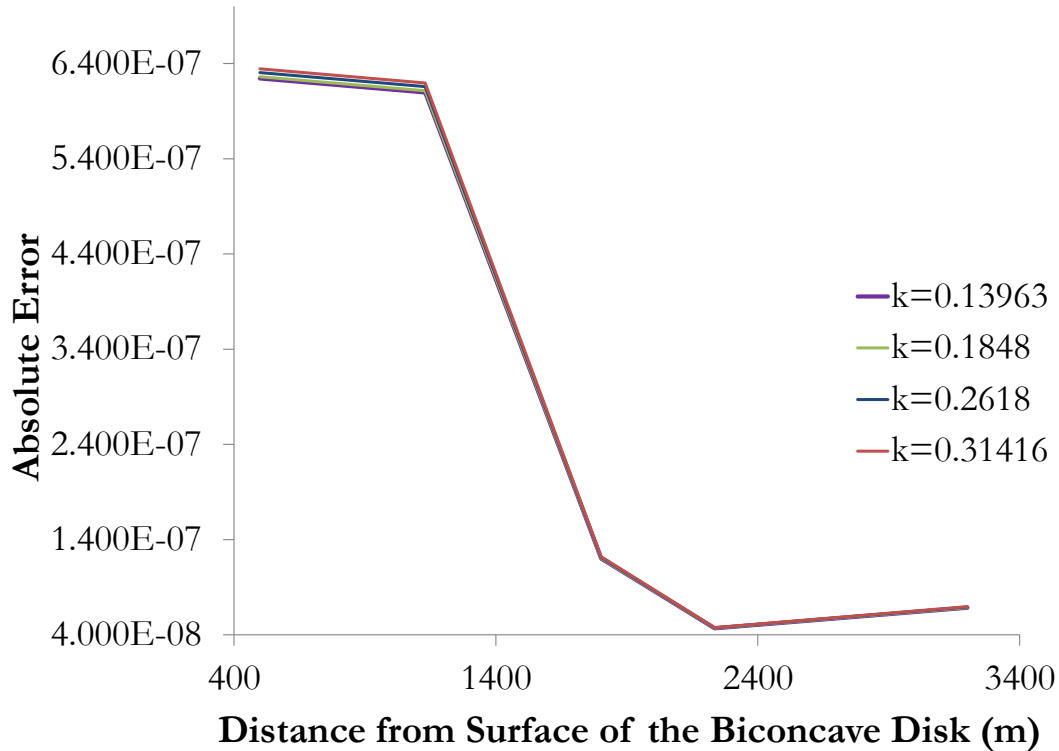
**Table 7.7.**  $N = 0, 15$  terms, degree is 5,  $A = 1$ ,  $B = 1$ ,  $C = 0.55$ ,  $\lambda = 1.4$ , 32 interior nodes, 20 exterior nodes,  $f_2(p)$  were used. Change in absolute error as the distance from the surface of the Biconcave Disk increases for different calculated  $k$ -values on planet Mars. In general, the absolute error decreases as distance increases. Also, absolute error decreases as wavenumber decreases for most points. The best point on the graph (highlighted in green) is near the smooth part of the Bloodcell.

Using the conditions determined by previous analyses using boundary function 2—degree of boundary function is 5 and node combination of 32,20—varying  $k$ -values are now tested (Table 7.7). Recall that wavenumbers that occur in the atmosphere on planet Mars were calculated in section 3. For the wavenumbers that were calculated in the lower two atmospheric layers of planet Mars, lower wavenumbers produce better convergence results for boundary function 2. Thus  $k = 0.13963$  produced the best convergence results. The wavenumber  $k = 0.13963$  occurs at the altitude of 110 km above the surface of planet Mars. the frequency at this altitude is relatively small at 0.393 Hz.

The wavenumber  $k = 0.31416$  occurs close to the surface of planet Mars and are the breaks between the atmospheric layers. This relatively high wavenumber occurs at elevations of 25 km, 65 km, and 135 km above the surface of planet Mars. These elevations also have relatively high frequencies of 1.07 Hz, 8.49 Hz, and 0.986, respectively. It is not surprising to see a sudden fluctuation in the frequencies exhibited at the volatile areas between the atmospheric layers and close to the surface.

The wavenumber  $k = 0.26180$  occurs at an elevation of 82 km above the surface of planet Mars and has a frequency of 0.645 Hz. The wavenumber  $k = 0.18480$  occurs at an elevation of 45 km above the surface of planet Mars and has a frequency of 0.591 Hz. These are the mid- range wavenumbers that were tested. These wavenumbers occur in the middle of the Troposphere and Mesosphere layers of the Mars atmosphere.

The last row of Graph 7.7 (highlighted in yellow) was included to demonstrate the effect that the orientation of the incoming wave has on convergence results for boundary function 2. The point coordination for this point is  $(4, 5, 0)$ , which is 5.4 meters from the surface of the Biconcave Disk. This point has the lowest absolute error from any other point in Table 7.7 because it is as far from radiating toward the depression as possible—the z-coordinate is 0.



**Graph 7.5.**  $N = 0, 15$  terms, degree of the boundary function is 5,  $A = 1$ ,  $B = 1$ ,  $C = 0.55$ ,  $\lambda = 1.4$ , 32 interior nodes, 20 exterior nodes,  $f_2(p)$  were used. Change in absolute error as the distance from the surface of the Biconcave Disk increases for different calculated  $k$ -values on planet Mars. The graph shows that while the smaller wavenumbers that were tested give better convergence results than larger wavenumbers that were tested, the difference is not significant. This is because all of the wavenumbers tested were relatively small.

It can be seen from testing various  $k$ -values on planet Mars that lower wavenumbers produce better results (Graph 7.5 for Table 7.7). However, all wavenumbers that occur on planet Mars are relatively low, so the convergence results for each wavenumber are all very good.

Now, we will choose the wavenumber,  $k = 10.904122$ , which is an eigenvalue of the interior Dirichlet problem. Then this will be used to compare the two boundary functions to each other (Table 7.8).

Distance from the Surface of the Biconcave Disk (m)	Absolute Error for $k = 10.904122$ with an Ellipsoidal Radius	
	Boundary Function 1	Boundary Function 2
190	$6.038D - 03$	$2.136D - 03$
499	$9.595D - 04$	$1.099D - 05$
639	$7.777D - 04$	$3.350D - 06$
640	$2.234D - 03$	$5.909D - 04$
706	$2.011D - 03$	$5.368D - 04$
3,000	$5.870D - 04$	$8.201D - 05$
3,606	$3.320D - 04$	$1.027D - 04$
3,742	$3.634D - 04$	$1.000D - 04$
5.4	$7.789D - 02$	$6.884D - 10$

**Table 7.8.**  $N = 0, 15$  terms, degree is 5,  $A = 1$ ,  $B = 1$ ,  $C = 0.55$ ,  $\lambda = 1.4$ , 32 interior nodes, 20 exterior nodes were used. Change in absolute error as the distance from the surface of the Biconcave Disk increases for the interior Dirichlet eigenvalue,  $k = 10.904122$ . In general, the absolute error decreases as distance increases. Also, absolute error is smaller at each point for boundary function 2 than boundary function 3.

Table 7.8 shows that at each point, boundary function 2 produces better convergence results than boundary function 1. The table also implies that the method is valid because the convergence results are still relatively good. Without using the Modified Galerkin method, the Helmholtz equation would break down at the eigenvalue. Thus we know that the method eliminates the possible problem that arises from the interior Dirichlet eigenvalue,  $k = 10.904122$ , and produces a good approximation at this wavenumber.

## 8. *Conclusion*

Boundary function 2 generally gave better results than boundary function 1. However, in the results for boundary function 2,  $f_2(p) = \frac{e^{ikr}}{r^2} \left(1 + \frac{i}{kr}\right) z$ , the smooth part of the boundary of the Biconcave Disk gives better convergence results compared to the results at the depression. Whereas, the boundary function  $f_1(p) = \frac{e^{ikr}}{r}$  does not show any difference in convergence results depending on the orientation of the incoming wave. Instead, the results for boundary function 1 only depended on the distance of the incoming wave from the surface of the Biconcave Disk. Thus, boundary function 1 provided more consistent results than boundary function 2, and boundary function 2 gave a wider range of convergence results, including some very good and others very poor.

The smaller wavenumbers tested tend to provide better convergence results than the larger wavenumbers tested; however, all wavenumbers tested were relatively small. Thus all wavenumbers gave good convergence results. It may be concluded then that the methods used were viable for analysis of waves in the atmosphere on planet Mars because wavenumbers were tested that occur in the lower two atmospheric layers on planet Mars and in the transition to the third atmospheric layer. Additionally, the atmosphere gets thinner in the third atmospheric layer as altitude from the surface of Mars increases, so the wavenumbers will continue to get smaller. This supports the claim that if wavenumbers in higher altitudes of the Mars atmosphere were calculated and tested, these will likely provide good convergence results.

As the number of terms,  $N$ , was increased, the convergence results exhibited no change. As the number of terms in the infinite series increased, the convergence results improved. When the degree of the boundary function was 5, usually the best convergence results were obtained. An ellipsoidal radius, while providing a closer radius approximation, generally produced no change in the convergence result. It is useful to look at the numerical results in light of the drag coefficient's effect on the surface of the Biconcave Disk to determine its best use in the design of a spacecraft



(Table 8.1).

Distance from the Surface of the Biconcave Disk (m)	Absolute Error for Wavenumbers for an Ellipsoidal Radius			
	0.13963	0.18480	0.26180	0.31416
500	1.562D-04	1.568D-04	1.582D-04	1.595D-04
3,000	2.604D-05	2.614D-05	2.637D-05	2.658D-05
499	6.243D-07	6.262D-07	6.306D-07	6.345D-07
499	6.243D-07	6.262D-07	6.306D-07	6.345D-07
639	1.903D-07	1.909D-07	1.923D-07	1.934D-07
5.4	1.532D-08	1.154D-08	8.093D-09	6.706D-09
1,130	8.813D-11	6.640D-11	4.656D-11	3.858D-11

**Table 8.1.**  $N = 0, 15$  terms, degree is 5,  $A = 1$ ,  $B = 1$ ,  $C = 0.55$ ,  $\lambda = 1.4$ , 32 interior nodes, 20 exterior nodes,  $f_2(p)$  were used. Absolute error for calculated k-values at various points around the surface of the Biconcave Disk. (red highlight) The results obtained from the points close to the “dip” in the Bloodcell suggest a high drag coefficient on that part of the surface. (blue highlight) The results obtained from the points close to the smooth portion of the Bloodcell suggest a low drag coefficient on that part of the surface.

Table 8.1 shows us that there is a wide variation in convergence results between points that radiate toward the depression (highlighted in red) and points that radiate toward the smooth portion (highlighted in blue) of the Biconcave Disk. This suggests that the drag coefficient is high near the depression and the drag coefficient is low around the smooth sphere-like portion of the Bloodcell. This validates our assumptions because the faces of the surface with a depression have a higher surface area that would be in contact with the atmospheric gasses than smoother sides of the Biconcave Disk would. When the goal is to minimize the drag coefficient, such as for taking off, the Biconcave Disk should be oriented “vertically” as part of a spacecraft. But when the goal is to maximize the drag coefficient, such as for landing, the Biconcave Disk should be oriented “horizontally” as part of a spacecraft. This way, the spacecraft would use the Biconcave Disk’s high drag coefficient area to produce a softer landing. Therefore, it is proposed that a rotation of the Biconcave Disk is necessary between landing and taking from planet Mars so the shape can overcome the drag coefficient upon taking off. The study of the drag coefficient also shows us that the best use of the Bloodcell as part of a spacecraft would be when it is attached to another part of the spacecraft at the dip.

It may be useful to note that Recktenwald (2008) observed similar drag coefficient patterns across a solid disk during simulations in a wind tunnel. Although the disk tested was simpler than the Biconcave Disk, Recktenwald reported increased drag coefficient with increased angle from the

”horizontal” position (Recktenwald, 2008).

After convergence results for the Dirichlet boundary condition for the Biconcave Disk are obtained. Then the Dirichlet boundary condition can be added to the Neumann boundary condition in a one to  $\mu$  ratio of reflection and absorption in order to expand this research to the Robin boundary condition.

Finally, after I found the best convergence results for the “ideal shape” of the Biconcave Disk, I designed a model of the Biconcave Disk. This is the final product of this thesis, which incorporates both of my major’s: mathematics and graphic design. I have designed the exterior of the Biconcave Disk based on the fundamentals of graphic design while incorporating the iconic look of NASA. This design includes a color-coded system which displays the areas that have a higher drag coefficient in a different color than the areas that have a lower drag coefficient.

## 9. *Possible Future Directions for this Work*

In the future, more terms from the infinite series can be added by increasing the value of  $N$ . Also, more equations for the boundary function  $f(p)$  can be tested (such as equations 3.3c). More Gaussian Quadrature nodes can be obtained and added to the program in Fortran 77. Then, the Gaussian Quadrature nodes can be used to test whether more interior nodes, more exterior nodes, or more of both will provide better convergence results than those already obtained. The aforementioned evaluations have not yet been performed due to the lack of processing power and lack of known nodes and terms.

Known materials that can be used for a spacecraft each have different absorption and reflection. Each material's absorption proportions can be tested for the Robin boundary condition. Further research can be conducted to investigate which part of the spacecraft is better suited for the Biconcave Disk. This will give a better view of how to design the Bloodcell shape for its specific use.

## 10. *Appendix A*

### *Definitions*

#### 10.1 **Basis**

A basis is a linearly independent set of vectors that generate the entire vector space. Each vector in the space is a finite linear combination of vectors in the basis.

For infinite space, we can interpret the Basis as the infinite linear combination of vectors  $\sum_{i=1}^{\infty} v_i$ . We consider the series of partial sums  $S_n = \sum_{i=1}^n v_i$  for  $n = 1, 2, 3, \dots$  and hope that this converges to some vector  $v$ .

A basis can be written as an orthonormal basis. This means that all the vectors in the basis are normalized to unit vectors and they are all orthogonal to each other. For example,  $(1,0,0)$ ,  $(0,1,0)$ ,  $(0,0,1)$  form an orthonormal basis for  $\mathbb{R}^3$

#### 10.2 **Bessel Functions**

Bessel functions are known as cylinder functions or cylindrical harmonics because they appear in the solution to Laplace's equation in cylindrical coordinates. They also arise in the Helmholtz equations in cylindrical or spherical coordinates. Important for problems of wave propagation. These are solutions  $q(p)$  to the Bessel differential equation  $p^2 \frac{d^2 q}{dp^2} + p \frac{dq}{dp} + (p^2 - \alpha^2)q = 0$  for an arbitrary complex number  $\alpha$ .

### 10.3 $C^{l,\lambda}$ space

This is a space of the continuous functions on  $S$ , the surface of the Biconcave Disk. A function  $f \in C^{l,\lambda}(S)$  if  $f$  is  $l$  times continuously differentiable and if the  $l^{th}$ -order derivatives are Hölder continuous with exponent  $\lambda$ . The norm for this space is  $\|f\|_\infty = \max_{p \in S} |f(p)|$ ,  $f \in C(S)$ .

Hölder continuous, when there are nonnegative real constants  $C$ ,  $\alpha$

, such that  $|f(p) - f(q)| \leq C \|p - q\|^\alpha$  for all  $p$  and  $q$  in the domain of  $f$ .

### 10.4 Hankel Functions

Also known as Bessel functions of the third kind. Hankel functions are linear combinations of Bessel functions of the first and second kinds. The Hankel functions of the first kind and of order  $n$  are  $h_n^{(1)} = j_n + iy_n$  and we only need to consider the Hankel functions of the first kind for our methods.

Where

$$\begin{aligned} j_n(z) &= \frac{\sqrt{\pi}}{2} \left(\frac{z}{2}\right)^{-1/2} J_{n+1/2}(z), \text{ where} \\ J_{n+1/2}(z) &= \sum_{k=0}^{\infty} \frac{(-1)^k (z/2)^{n+2k+1/2}}{k! \Gamma(n+k+1+1/2)}, \\ y_n(z) &= \frac{\sqrt{\pi}}{2} \left(\frac{z}{2}\right)^{-1/2} Y_{n+1/2}(z), \text{ where} \\ Y_{n+1/2}(z) &= \frac{J_{n+1/2}(z) \cos(z\pi) - J_{-(n+1/2)}(z)}{\sin(z\pi)}, \\ \text{and } h_n^{(1)}(z) &= \frac{\sqrt{\pi}}{2} \left(\frac{z}{2}\right)^{-1/2} H_{n+1/2}^{(1)}(z) \end{aligned}$$

Hankel functions often have a factor of the form  $e^{if(x)}$ . Hankel functions are used to express outward and inward propagating cylindrical wave solutions of the cylindrical wave equation.

### 10.5 Infinite Space

This is a space with infinite dimensions. In general, this is defined on Euclidian space on infinite space, we sometimes need to go about it differently because the dimensions are not countable.

There is a distance function between points in infinite space, there are angles between vectors. We can find the distance between functions in the space by using inner product.

*Example of Infinite Space*

the norm is  $\|x\|_p = \left( \sum_{i \in \mathbb{N}} |p_i|^n \right)^{1/n}$  where  $n$  can be uncountable i.e. infinity.

## 10.6 Jacobian

The Jacobian is the determinant of the Jacobian matrix, which is composed of partial derivatives of each transition function with respect to the new variables the graph is mapped to. The Jacobian

finds the transformation of the integral operator in the new domain. For  $\left\{ \begin{array}{l} q_1 = f_1(p_1, \dots, p_n) \\ \vdots \\ q_n = f_n(p_1, \dots, p_n) \end{array} \right\}$ ,

$$J(p_1, \dots, p_n) = \begin{bmatrix} \frac{\partial q_1}{\partial p_1} & \dots & \frac{\partial q_1}{\partial p_n} \\ \vdots & \ddots & \vdots \\ \frac{\partial q_n}{\partial p_1} & \dots & \frac{\partial q_n}{\partial p_n} \end{bmatrix}. \quad J = \|\partial(q_1, \dots, q_n) \partial(p_1, \dots, p_n)\|.$$

## 10.7 Legendre Functions

$p_n(u)$  and  $p_n^m(u)$  denote the Legendre polynomials and associated Legendre functions on  $[-1, 1]$ ,

$$n \geq 0, \quad 1 \leq m \leq n,$$

$$p_n(u) = \frac{1}{2^n n!} \frac{d^n (u^2 - 1)^n}{du^n} \quad \text{and}$$

$$p_n^m(u) = \frac{1}{2^n n!} (1 - u^2)^{m/2} \frac{d^{m+n} (u^2 - 1)^n}{dt^{m+n}}$$

$$(-n \leq m \leq n).$$

## 10.8 Norm

Norm of a space gives the length of a vector, or it defines the distance function on the space. It is a function that maps points in  $X$  to distance between points  $\mathbb{R}$ . Where  $X$  has a norm in the space is in.

## 10.9 Smoothness

A boundary of a surface is smooth if it is continuously differentiable on the boundary: the surface,  $S$ , is smooth if  $r'$  is continuous and nonzero on the boundary of  $S$ .

## 10.10 Uniform Continuity

Let  $S$  be a non-empty subset of  $\mathbb{R}$  and  $f : S \rightarrow \mathbb{R}$  is a real-valued function on  $S$ . Then  $f$  is uniformly continuous on  $S$  iff

$$\forall \varepsilon > 0 \exists \delta > 0$$

that  $\forall p_0 \in S$  and  $\forall p \in S$

if  $(p - p_0) < \delta$  then  $|f(p) - f(p_0)| < \varepsilon$ .

## 10.11 Uniform Convergence

On the coefficients  $a_{nm}$ , we impose the condition that the series  $\chi(p, q)$  is uniformly convergent in  $p$  and in  $q$  in any region  $|p|, |q| > R + \epsilon$ ,  $\epsilon > 0$ , and that the series can be two times differentiated term by term with respect to any of the variables with the resulting series being uniformly convergent. We also assume that the series  $\chi$  is a solution of the Helmholtz equation satisfying the Sommerfeld radiation condition for  $|p|, |q| > R$

## 11. Appendix B

### *Proofs and Examples*

#### 11.1 Proof of Spherical Harmonic Basis

**Theorem 2** *Every sequence of spherical harmonics that converges is bounded.*

**Proof.** Suppose  $T$  is a sequence of spherical harmonics that is convergent to a number  $\mu$ .

For  $\varepsilon = 1$ , there is a natural number  $N$  such that if  $n > N$ , then

$$|T_n - \mu| < 1.$$

$$|T_n - \mu| = |-(T_n - \mu)| = |\mu - T_n| \text{ so } |\mu - T_n| < 1.$$

Since  $||T_n| - |\mu|| \leq |T_n - \mu|$  we have for all  $n > N$ ,  $|T_n| - |\mu| < 1$ .

Thus for all  $n > N$ ,  $|T_n| < 1 + |\mu|$ .

All but the first  $N$  terms are bounded by  $1 + |\mu|$ . Now we consider the first terms.

$$\text{Let } \max\{|T_1|, |T_2|, \dots, |T_N|, 1 + |\mu|\} = \frac{C}{N^{l+\lambda}}.$$

Then  $|T_n| \leq \frac{C}{N^{l+\lambda}}$  for all  $n \in \mathbb{N}$ , and  $T$  is bounded. ■

#### 11.2 Proof of Galerkin's Weighted Residual Method

The following is a specific example of the weighted residual method. It serves as a demonstration of the method behind the Galerkin's weighted residual method used in the calculations for the weights in the Modified Galerkin Method. The integral equation used in the methods is a Fredholm integral of the second kind. Additionally, the basis chosen in the methods is a basis of spherical harmonics.

**Proposition 3** *For the equation  $\frac{\partial^2 \varphi}{\partial x^2} = x + 1 : 0 < x < 1$  with the boundary conditions:  $\varphi|_{x=0} = 0$ ,*



$\varphi|_{x=1} = 1$ , one can choose any linearly independent basis of the form  $\{1, x, x^2, \dots, x^n\}$  for  $n \in \mathbb{N}$  and find a solution of the form  $\varphi(x) = c_1 + c_2x + c_3x^2 + c_4x^3 + \dots + c_nx^{n-1} + c_{n+1}x^n$ .

**Proof.** Base case: Suppose  $n = 1$ . Then the basis is  $\{1, x\}$  and the solution is of the form  $\varphi(x) = c_1 + c_2x$ .

Plugging in the boundary conditions, we get  $\varphi(0) = c_1 = 0$  and  $\varphi(1) = c_1 + c_2 = 1$ , which implies  $c_2 = 1$ .

So the solution is  $\varphi(x) = x$ .

Since this case did not use the Galerkin method of weighted residuals, we will now consider the base case of  $n = 2$ .

Suppose  $n = 2$ . Then the basis is  $\{1, x, x^2\}$  and the solution is of the form  $\varphi(x) = c_1 + c_2x + c_3x^2$ .

Plugging in the boundary conditions, we get  $\varphi(0) = c_1 = 0$  and  $\varphi(1) = c_1 + c_2 + c_3 = 1$ , which implies  $c_2 + c_3 = 1$ .

So the solution is of the form  $\varphi(x) = c_2x + c_3x^2$ .

Taking the first and second derivatives of this function, we get  $\varphi'(x) = c_2 + 2c_3x$  where  $C \in \mathbb{R}$  and  $\varphi''(x) = 2c_3$ .

We know that  $\int_0^1 w_i \left( \frac{d^2\varphi}{dx^2} - x - 1 \right) dx = 0$  where  $w_1 = x - x = 0$  and  $w_2 = x^2 - x$ .

So for  $w_1$ :  $\int_0^1 (0) (2c_3 - x - 1) dx = 0$

And for  $w_2$ :  $\int_0^1 (x^2 - x) (2c_3 - x - 1) dx = 0$

$\Rightarrow \int_0^1 (-x^3 + 2c_3x^2 + (1 - 2c_3)x) dx = 0$

$\Rightarrow \left[ -\frac{x^4}{4} + 2c_3\frac{x^3}{3} + (1 - 2c_3)\frac{x^2}{2} \right]_0^1 = 0$

$\Rightarrow -\frac{1}{4} + 2c_3\frac{1}{3} + (1 - 2c_3)\frac{1}{2} = 0$

$\Rightarrow \frac{1}{4} - \frac{c_3}{3} = 0$

So  $c_3 = \frac{3}{4}$  and since  $c_2 + c_3 = 1$  that means  $c_2 = \frac{1}{4}$ .

Now we know the solution is  $\varphi(x) = \frac{1}{4}x + \frac{3}{4}x^2$ .

Induction: Now let us assume that for the equation  $\frac{\partial^2\varphi}{\partial x^2} = x + 1$ :

$0 < x < 1$  with the boundary conditions:  $\varphi|_{x=0} = 0$ ,  $\varphi|_{x=1} = 1$ , one can choose any linearly independent basis of the form  $\{1, x, x^2, \dots, x^{k-1}\}$  for up to some  $k - 1 \in \mathbb{N}$ .

Now, consider the case when the basis is  $\{1, x, x^2, \dots, x^{k-1}, x^k\}$ .

The solution is of the form:  $\varphi(x) = c_1 + c_2x + c_3x^2 + c_4x^3 + \dots + c_kx^{k-1} + c_{k+1}x^k$ .

Using the initial conditions, we find that:  $\varphi(0) = c_1 = 0$

$$\varphi(1) = c_1 + c_2 + c_3 + \dots + c_{k+1} = 1$$

$$= c_2 + c_3 + \dots + c_{k+1} = 1$$

$$\Rightarrow c_2 = 1 - c_3 - c_4 - \dots - c_{k+1}$$

Now the solution is written as:

$$\varphi(x) = (1 - c_3 - c_4 - \dots - c_{k+1})x + c_3x^2 + \dots + c_{k+1}x^k = x + c_3(x^2 - x) + c_4(x^3 - x) + \dots + c_k(x^{k-1} - x)$$

And we can take the first and second derivative of this function

$$\varphi'(x) = 1 + c_3(2x - 1) + c_4(3x^2 - 1) + \dots + c_k((k-1)x^{k-2} - 1)$$

$$\varphi''(x) = 2c_3 + 6c_4x + \dots + (k-1)(k-2)c_kx^{k-3}$$

We know that the weighted residual is:

$$\int_0^1 w_i \left( \frac{d^2\varphi}{dx^2} - x - 1 \right) dx = 0 \text{ where } w_1 = x^2 - x, w_2 = x^3 - x, \dots, w_{k-2} = x^{k-1} - x$$

So for  $w_1$  we have:

$$\int_0^1 (x^2 - x) (2c_3 + 6c_4x + \dots + (k-1)(k-2)c_kx^{k-3} - x - 1) dx = 0$$

$$\int_0^1 (2c_3x^2 + 6c_4x^3 + \dots + (k-1)(k-2)c_kx^{k-1} - x^3 - x^2 - 2c_3x - 6c_4x^2 - \dots - (k-1)(k-2)c_kx^{k-2} + x^2 + x) dx = 0$$

$$\int_0^1 ((1 - 2c_3)x + (2c_3 - 6c_4)x^2 + (6c_4 - 12c_5 - 1)x^3 + \dots + ((k-2)(k-3)c_{k-1} - (k-1)(k-2)c_k)x^{k-2} + (k-1)(k-2)c_kx^{k-1}) dx = 0$$

$$\left[ (1 - 2c_3)\frac{x}{2} + (2c_3 - 6c_4)\frac{x^3}{3} + (6c_4 - 12c_5 - 1)\frac{x^4}{4} + \dots + ((k-2)(k-3)c_{k-1} - (k-1)(k-2)c_k)\frac{x^{k-1}}{k-1} + (k-1)(k-2)c_k\frac{x^k}{k} \right]_0^1 = 0$$

$$\frac{1}{4} - \frac{1}{3}c_3 - \frac{1}{2}c_4 - \frac{3}{5}c_5 - \dots - \frac{k-2}{k}c_k = 0$$

Similarly for  $w_2$  we have:

$$\int_0^1 (x^3 - x) (2c_3 + 6c_4x + \dots + (k-1)(k-2)c_k x^{k-3} - x - 1) dx = 0$$

$$\text{and } \frac{23}{60} - \frac{1}{2}c_3 - \frac{4}{5}c_4 - c_5 - \dots - \left[ \frac{k-1}{k+1} - 1 \right] (k-2)c_k = 0$$

...

And we know we can set up the weighted residual integrals up to  $w_{k-3}$ .

Then for  $w_{k-2}$  we have:

$$\int_0^1 (x^{k-1} - x) (2c_3 + 6c_4x + \dots + (k-1)(k-2)c_k x^{k-3} - x - 1) dx = 0$$

so

$$\frac{5k^2 - 7k - 6}{6k(k+1)} + \left( \frac{2}{k} - 1 \right) c_3 + \left( \frac{6}{k+1} - 2 \right) c_4 + \dots - (k-2)c_k + \dots + (k-1)(k-2) \frac{c_k}{k-3} = 0$$

Which gives us a system of  $k-2$  equations:

$$\left\{ \begin{array}{l} \frac{1}{4} - \frac{1}{3}c_3 - \frac{1}{2}c_4 - \frac{3}{5}c_5 - \dots - \frac{n-2}{n}c_n = 0 \\ \frac{23}{60} - \frac{1}{2}c_3 - \frac{4}{5}c_4 - c_5 - \dots - \left[ \frac{n-1}{n+1} - 1 \right] (n-2)c_n = 0 \\ \vdots \\ \frac{5n^2 - 7n - 6}{6n(n+1)} + \left( \frac{2}{n} - 1 \right) c_3 + \left( \frac{6}{n+1} - 2 \right) c_4 + \dots - (n-2)c_n + \dots + (n-1)(n-2) \frac{c_n}{n-3} = 0 \end{array} \right.$$

This system of equations has  $k-2$  unknown constants. We know we can solve a system of  $k-3$  equations for  $k-3$  unknown constants, thus we can solve this system for  $k-2$  unknown constants. The solution is of the form  $\varphi(x) = c_2x + c_3x^2 + c_4x^3 + \dots + c_kx^{k-1} + c_{k+1}x^k$ , where  $c_2 = 1 - c_3 - c_4 - \dots - c_{k+1}$ , and all other  $c_i$  are found by solving the above system. ■

### 11.3 Example: Adomian Decomposition Method

This method provides a solution for a wide class of both integral and differential equations. The solution,  $u(x)$ , is provided in a series form by the following equation:

$$u(x) = \sum_{n=0}^{\infty} u_n(x).$$

This decomposition is a solution to a Fredholm integral equation given by:

$$\sum_{n=0}^{\infty} u_n(x) = f(x) + \lambda \int_a^b K(x,t) \left( \sum_{n=0}^{\infty} u_n(t) \right) dt.$$

The integral equation can be written in a recursive manner by

$$u_0(x) = f(x)$$

$$u_{n+1}(x) = \lambda \int_a^b K(x,t) u_n(t) dt, \quad n \geq 0.$$

To demonstrate this method, we will consider the following example.

**Example 4** Consider the Fredholm integral equation of the second kind

$$u(x) = 1 + \sec^2(x) - \int_0^{\pi/4} u(t)dt$$

Now we use the recursive scheme to evaluate  $u_0(x), u_1(x), u_2(x), \dots$

$$u_0(x) = 1 + \sec^2(x)$$

$$u_1(x) = - \int_0^{\pi/4} u_0(t)dt$$

$$= - \int_0^{\pi/4} 1 + \sec^2(t)dt$$

$$= - [t + \tan(t)]_0^{\pi/4}$$

$$= - \left( \frac{\pi}{4} + 1 \right) = -\frac{5\pi}{4}$$

$$u_2(x) = - \int_0^{\pi/4} u_1(t)dt$$

$$= - \int_0^{\pi/4} -\frac{5\pi}{4} dt$$

$$= \left[ \frac{5\pi}{4} t \right]_0^{\pi/4} = \frac{5\pi^2}{16}$$

and so on. So the solution can be written as

$$u(x) = 1 + \sec^2(x) - \frac{5\pi}{4} + \frac{5\pi^2}{16} + \dots$$

Which can be represented as the geometric series

$$u(x) = -4 + \sec^2(x) + \sum_{n=0}^{\infty} 5 \left( -\frac{\pi}{4} \right)^n = -3 + \sec^2(x)$$

This is a closed form.

## 11.4 Example of the Modified Decomposition method

This method serves as a slightly easier implementation of the Adomian decomposition method, however the Modified Decomposition method does not work in every case. The Modified Decomposition is recommended for cases where the nonhomogeneous part consists of a combination of many terms. We begin by splitting the given function  $f(x)$  into two parts defined by

$$f(x) = f_0(x) + f_1(x)$$

where  $f_0(x)$  consists of a number of terms of  $f(x)$  and  $f_1(x)$  includes the remaining terms of  $f(x)$ .

The integral equation becomes

$$u(x) = f_0(x) + f_1(x) + \lambda \int_a^b K(x,t)u(t)dt, \quad a \leq x \leq b.$$

We use the expansion for the Adomian Decomposition method

$$\sum_{n=0}^{\infty} u_n(x) = f_0(x) + f_1(x) + \lambda \int_a^b K(x, t) \left( \sum_{n=0}^{\infty} u_n(t) \right) dt.$$

The integral equation can be written in a recursive manner by

$$u_0(x) = f_0(x),$$

$$u_1(x) = f_1(x) + \lambda \int_a^b K(x, t) u_0(t) dt,$$

$$u_{n+1}(x) = \lambda \int_a^b K(x, t) u_n(t) dt, \quad n \geq 1.$$

To demonstrate this method, we will consider the following example.

**Example 5** Consider the Fredholm integral equation:

$$f(x) = \frac{1}{\sqrt{1-x^2}} + (e^{\pi/6} - 1)x - x \int_0^{1/2} e^{\arcsin t} u(t) dt$$

To apply the Modified Decomposition method, we split the function  $f(x)$  into

$$f_0(x) = \frac{1}{\sqrt{1-x^2}}$$

$$f_1(x) = (e^{\pi/6} - 1)x$$

Then we set

$$u_0(x) = \frac{1}{\sqrt{1-x^2}} \text{ and}$$

$$\begin{aligned} u_1(x) &= (e^{\pi/6} - 1)x + x \int_0^{1/2} e^{\arcsin t} u_0(t) dt \\ &= (e^{\pi/6} - 1)x + x \int_0^{1/2} \frac{e^{\arcsin t}}{\sqrt{1-t^2}} dt \\ &= (e^{\pi/6} - 1)x + x [e^{\arcsin t}]_0^{1/2} \\ &= (e^{\pi/6} - 1)x + x [e^{\pi/6} - 1] = 0 \end{aligned}$$

It follows that the components  $u_n(x) = 0$  for  $n \geq 1$ . Then the exact solution is  $u(x) = \frac{1}{\sqrt{1-x^2}}$ .



## 12. *Appendix C*

### *Figures*

Original altitude (km)	Corrected altitude (km)	Atmospheric density (kg m <sup>-3</sup> )	Atmospheric pressure (mbar)	Atmospheric temperature (K)
120.00	117.61	1.60E-8	4.14E-6	136.3
116.00	113.65	2.42E-8	6.91E-6	149.2
112.00	109.70	3.95E-8	1.12E-5	148.6
108.00	105.75	6.59E-8	1.84E-5	146.4
104.00	101.79	1.06E-7	3.03E-5	149.4
100.00	97.84	1.67E-7	4.94E-5	154.8
96.00	93.89	2.88E-7	8.02E-5	145.9
92.00	89.93	5.39E-7	1.38E-4	133.6
88.00	85.98	8.33E-7	2.33E-4	146.7
84.00	82.03	1.40E-6	3.87E-4	144.2
80.00	78.07	2.57E-6	6.70E-4	136.6
76.00	74.12	4.66E-6	1.16E-3	130.5
72.00	70.17	7.70E-6	2.05E-3	139.1
68.00	66.21	1.17E-5	3.43E-3	152.9
64.00	62.26	1.88E-5	5.55E-3	154.6
60.00	58.31	3.19E-5	9.11E-3	149.5
56.00	54.35	5.96E-5	1.56E-2	136.8
52.00	50.40	9.56E-5	2.67E-2	146.3
48.00	46.44	1.57E-4	4.45E-2	148.6
44.00	42.49	2.65E-4	7.46E-2	147.5
40.00	38.54	4.10E-4	1.23E-1	157.4
36.00	34.58	6.25E-4	1.98E-1	166.1
32.00	30.63	9.32E-4	3.12E-1	175.1
28.00	26.68	1.38E-3	4.83E-1	183.8

**Table 12.1.** A data table from the report on atmospheric readings from NASA's Viking Lander 1 mission versus the corrected altitudes from the Mars Orbiter Laser Altimeter mission (MOLA). This table is abridged from the complete atmospheric data set obtained from the Viking Lander mission; however, it shows the adjusted altitudes from the MOLA mission. The atmospheric pressure and density shown in this table are important to the calculation of the wavenumber.

```

      SUBROUTINE SURFAC(X,Y,Z,DX,DY,DZ,IFLAG)
C
C   DX(1) IS TO CONTAIN THE DERIVATIVE OF X(PHI,THETA) WITH RESPECT
C   TO PHI UPON EXIT, AND DX(2) IS TO CONTAIN THE DERIVATIVE WITH
C   RESPECT TO THETA.
C
      IMPLICIT DOUBLE PRECISION(A-H,O-Z)
      COMMON/SURPAR/A,B,C,SNT,CST,SNP,CSP,NUMSUR
      DIMENSION DX(2),DY(2),DZ(2)
      DATA ZERO/0.0D0/,ONE/1.0D0/,TWO/2.0D0/
      GO TO (10,20),NUMSUR
C   THIS IS A Biconcave Disc REGION.
10   X=A*CSP*SNT
      Y=B*SNP*SNT
C     Z=C*CST
      Z=C*(0.3+0.7*SNT)*CST
      IF(IFLAG .EQ. 0) RETURN
      DX(1)=-A*SNT*SNP
      DX(2)=A*CSP*CST
      DY(1)=B*CSP*SNT
      DY(2)=B*SNP*CST
      DZ(1)=ZERO
C     DZ(2)=-C*SNT
      DZ(2)=C*(-(0.3+0.7*SNT)*SNT+CST*CST*0.7)
      RETURN

```

**Figure 12.1.** The portion of the Modified Galerkin method with the Biconcave Disk region programmed. The constants  $A$ ,  $B$ , and  $C$  are defined in another file.  $X$ ,  $Y$ , and  $Z$  are functions of phi and theta. The partial derivatives of each of these functions can be taken with respect to phi and theta, corresponding to (1) and (2), respectively. The partial derivatives are important in calculation of the Jacobian.



```

SUBROUTINE ZEROLG(N,ZZ,WW,A,B)
C
C PRODUCE THE NODES AND WEIGHTS FOR GAUSS-LEGENDRE QUADRATURE
C ON (A,B), OF ORDER N. THE NUMBER OF NODES N IS RESTRICTED TO
C BE .LE. 20.
C
      IMPLICIT DOUBLE PRECISION(A-H,O-Z)
      DIMENSION Z(109),W(109),ZZ(N),WW(N)
      DATA ONE/1.0D0/,TWO/2.0D0/
      DATA Z(1),Z(2),Z(3),Z(4),Z(5),Z(6),Z(7),Z(8),Z(9),Z(10)/
*.577350269189626D0,.774596669241483D0,0.0D0,.861136311594053D0,
*.339981043584856D0,.906179845938664D0,.538469310105683D0,0.0D0,
*.932469514203152D0,.661209386466265D0/
      DATA Z(11),Z(12),Z(13),Z(14),Z(15),Z(16),Z(17),Z(18),Z(19),Z(20)/
*.238619186083197D0,.949107912342759D0,.741531185599394D0,
*.405845151377397D0,0.0D0,.960289856497536D0,.796666477413627D0,
*.525532409916329D0,.183434642495650D0,.968160239507626D0/
      DATA Z(21),Z(22),Z(23),Z(24),Z(25),Z(26),Z(27),Z(28),Z(29)/
*.836031107326636D0,.613371432700590D0,.324253423403809D0,
*.0D0,.973906528517172D0,.865063366688985D0,.679409568299024D0,
*.433395394129247D0,.148874338981631D0/
      DATA Z(30),Z(31),Z(32),Z(33),Z(34),Z(35),Z(36),Z(37),Z(38)/
*.978228658146057D0,.887062599768095D0,.730152005574049D0,
*.519096129206812D0,.269543155952345D0,0.0D0,
*.981560634246719D0,.904117256370475D0,.769902674194305D0/
      DATA Z(39),Z(40),Z(41),Z(42),Z(43),Z(44),Z(45),Z(46),Z(47)/
*.587317954286617D0,.367831498998180D0,.125233408511469D0,
*.984183054718588D0,.917598399222978D0,.801578090733310D0,
*.642349339440340D0,.448492751036447D0,.230458315955135D0/
      DATA Z(48),Z(49),Z(50),Z(51),Z(52),Z(53),Z(54),Z(55),Z(56)/
*.0D0,.986283808696812D0,.928434883663574D0,
*.827201315069765D0,.687292904811685D0,.515248636358154D0,
*.319112368927890D0,.108054948707344D0,.987992518020485D0/
      DATA Z(57),Z(58),Z(59),Z(60),Z(61),Z(62),Z(63),Z(64),Z(65)/
*.937273392400706D0,.848206583410427D0,.724417731360170D0,
*.570972172608539D0,.394151347077563D0,.201194093997435D0,

```

**Figure 12.2.** This is a portion of the program in which the nodes and weights are programmed. From these nodes and weights, the Galerkin coefficients are calculated. The weights and nodes are calculated using the Gaussian Quadrature method. The values  $Z$  are the nodes and the values  $W$  (not shown in this figure) are the weights. The nodes in the Gauss quadrature function for  $[-1, 1]$  are defined as the roots of the Legendre polynomial for  $n$ :  $P_n(z) = \frac{1}{2\pi_i} \int_{-1}^1 (1 - 2tz + r^2)^{-1/2} t^{-n-1} dt$ . Where the weights  $w_i$  come from the following function:  $w_i = -\frac{1}{(1 - z_i^2)[P'_i(z_i)]^2}$ .

. The program lists the weights and nodes for  $n = 2$  through  $n = 32$ .

## 13. *References*

- [1] Dinh, H. (2015). The numerical solution of the exterior impedance (Robin) problem for the Helmholtz's equation via modified galerkin method: Superellipsoid. Roger Williams University Thesis Collection.
- [2] Frank, J. E. (n.d.). Collocation Methods.
- [3] Kleinman, R. E., and Roach, G. F. (1982). On modified green functions in exterior problems for the Helmholtz equation. Proceedings of the Royal Society of London. Series A, Mathematical and Physical Sciences.
- [4] Kropinski, M. A., and Quaife, B. (2010). Fast integral equation methods for the modified Helmholtz equation. Journal of Computational Physics.
- [5] Lin, T. C., and Warnapala, Y. (2002). The numerical solution of the exterior Dirichlet problem for Helmholtz's equation via modified green's functions approach. Computers and Mathematics with Applications.
- [6] Lin, T. C., and Warnapala, Y. (2004). The numerical solution of the exterior Neumann problem for Helmholtz's equation via modified green's functions approach. Computers and Mathematics with Applications.
- [7] Magalhães, J. A., Schofield, J. T., and Seiff, A. (1999). Results of the Mars Pathfinder atmospheric structure investigation. Journal of Geophysical Research.
- [8] Recktenwald, B. (2008). Aerodynamics of a circular planform aircraft. American Institute of Aeronautics and Astronautics.
- [9] Süli, E. (2012). Lecture notes on finite element methods for partial differential equations.
- [10] Warnapala, Y., and Morgan, E. (2008). The numerical solution of exterior Dirichlet problem for Helmholtz's equation via modified green's functions approach for the oval of Cassini. Far East Journal of Applied Mathematics.

- [11] Warnapala, Y., Siegel, R., and Pleskunas, J. (2011). The numerical solution of the exterior boundary value problems for the Helmholtz's equation for the pseudosphere. *IAENG International Journal of Applied Mathematics*.
- [12] Warnapala, Y., and Dinh, H. (2013). Numerical solution of the Helmholtz equation for the superellipsoid via the galerkin method. *Communications in Numerical Analysis*.
- [13] Warnapala, Y., and Dinh, H. (2014). The modified galerkin method for the modified wave equation for the shape of superellipsoid. *British Journal of Mathematics and Computer Science*.
- [14] Warnapala, Y., Dinh, H., and Resh, J. (2015). The modified galerkin method for solving the Helmholtz equation for low frequencies on planet mars. *Asian Journal of Fuzzy and Applied Mathematics*.
- [15] Weisstein, E. W. (n.d.). Laplace's equation, *MathWorld-A Wolfram Web Resource*.
- [16] Withers, P., Lorenz, R. D., and Neumann, G. A. (2002). Comparison of Viking lander descent data and MOLA topography reveals kilometer-scale offset in Mars atmosphere profiles. *Elsevier Science*.